Energy 329 (2025) 136629

Contents lists available at ScienceDirect

Energy

journal homepage: www.elsevier.com/locate/energy

Thermal-electrical analysis of a novel interconnection for hybrid busbars in electric vehicle batteries

D.P.M. da Costa [a], M.M. Kasaei [b,*], R.J.C. Carbas [a,b], E.A.S. Marques [a], R.F.V. Sampaio [c], I.M.F. Bragança [c,d], L.F.M. da Silva [a]

[a] Department of Mechanical Engineering, Faculty of Engineering, University of Porto, Porto, Portugal
[b] Institute of Science and Innovation in Mechanical and Industrial Engineering (INEGI), Porto, Portugal
[c] IDMEC, Instituto Superior Técnico, Universidade de Lisboa, Portugal
[d] CIMOSM, Instituto Superior de Engenharia de Lisboa, Instituto Politécnico de Lisboa, Portugal

ARTICLE INFO

Handling editor: X Ou

Keywords:
Electric vehicle batteries
Hybrid busbars
Hole hemmed joints
Thermal-electrical analysis
Electrical resistance

ABSTRACT

Reliable and efficient busbar connections are critical for electric vehicle battery performance, yet conventional joining methods struggle with joining dissimilar materials such as copper and aluminum. This paper investigates a novel solution for joining hybrid copper-aluminum busbars using a technique called hole hemming, which eliminates the need for heating or additional elements. The focus is placed on the thermal-electrical performance of hole-hemming joints. Two configurations are studied: joints with and without branches. Numerical models analyse how sheet thickness affects temperature, electric current density, electric potential, and resistance, including models with cantered holes to study hole inclusion effects. Experimental tests are conducted on material strips and unit cells to assess electrical resistance changes with temperature and the effect of Joule heating on joint configurations. Compression using a hydraulic press is applied to improve contact, leading to significant electrical resistance improvements (78 % reduction for branched joints and 36 % for branchless ones). Mechanical shear tests before and after compression show a peak shear load of 4.54 kN and 13.84 mm displacement for branched joints, with slightly lower values for branchless joints. Despite a minor decrease in mechanical performance after compression, the improved thermal-electrical performance of the joints outweighs this. The findings highlight the promising potential of hole-hemmed joints for enhancing hybrid busbar connections.

1. Introduction

Nowadays, the global shift towards zero- and low-emission vehicles (ZLEVs) is highly noticeable [1–4]. Due to tighter and more severe regulations regarding carbon emissions, a constant evolution in electric vehicles (EVs) technology has been observed over the last few years, namely at the automotive battery pack level [5–7]. The Lithium-ion battery packs of EVs comprise an extensive network of interconnected cells designed to store electrical energy for the propulsion of electric motor(s) within an Electric Vehicle (EV). These packs consist of individual battery cells arranged into modules, which are subsequently assembled to form a unified pack [8].

In the domain of electric vehicles, the conveyance of electrical power commonly relies on a combination of cables, wires, and busbars. Busbars are metallic strips or sheets used to distribute electric power to switchgear systems [9,10] and are preferred in low voltage scenarios characterized by higher electric currents, typically forming parallel circuits [11]. They are the better option when compared to cable use regarding the circuit conditions above-mentioned. Busbars offer streamlined installation and maintenance processes, superior heat dissipation capabilities to prevent overheating, ensuring robust safety measures, and generally presenting cost-effectiveness [12].

Given the battery is one very expensive component of EVs, its nuances are of extreme relevancy. Besides the highly pertinent EV battery lifetime factor, addressed by Rücker et al. [13], one other impactful aspect of these relies on the performance under heating conditions [14–17]. Regarding heat dissipation, because of mid-to-high electric current applications, busbars need to provide good qualities in this matter. The joule heat generation that causes temperature rise in busbars in such applications is of significant importance. This thermal effect bears the potential to profoundly impact the thermal-electrical performance and may, in certain instances, be linked to operational failures [9,

* Corresponding author.
E-mail address: mkasaei@inegi.up.pt (M.M. Kasaei).

https://doi.org/10.1016/j.energy.2025.136629
Received 15 November 2024; Received in revised form 28 March 2025; Accepted 16 May 2025
Available online 21 May 2025

18,19]. Although of great matter, these kinds of thermal-electrical performance studies of busbars, namely hybrid busbars, aren't very common. Some authors, namely Kim et al. [20] have previously performed a thermal-electrical finite element analysis to determine heat dissipation in high-power switchboard applications. They focused on shape modification and surface treatment of copper, bearing in mind they did it on singular material busbars. Regarding hybrid busbars, fabricated from aluminium and copper, only a few have opted to thoroughly study the thermal-electrical performance of different joining methods. Sampaio et al. [9] manufactured and thermal-electrically studied fastened, friction stir spot welded, sheet-bulk compressed, and injection lap riveted joints, all made from aluminium and copper conductors. Their material selection always regarded the needed mechanical properties but was highly influenced by the great electrical and thermal characteristics of the materials, since they play an extremely vital role in these kinds of electric vehicle applications.

Regarding the joining processes in the scope of automotive battery systems manufacturing, the use of fasteners and some welding techniques is still an efficient option for a lot of battery pack systems manufacturing, although falling out of fashion due to new-electric power applications becoming increasingly smaller and more complex [12]. Moreover, fasteners add weight and volume and are usually made from materials with poor electrical conductivity. The use of rivets, nuts, and bolts provides reliable and easy-to-assemble/disassemble joints, although tending to manufacture current flow distorted joints because of non-uniform contact pressure [12]. There are several major and ground-breaking/emerging methods that have been used for quite some time now. Ultrasonic, laser, resistance spot welding, and joining by forming processes stand out for their applicability, and some, for their ground-breaking achievements [21].

Ultrasonic welding or ultrasonic metal welding (UMW) is one very commonly used joining method for this type of applications [22]. A high frequency ultrasonic energy source induces shear forces that oscillate, producing a bond, under clamping pressure. It can be done with a broad scope of materials [23]. Although only suitable for pouch cells, it is a fast process that results in high-strength and low-resistance joints. Resistance spot welding's main trait is that it allows for the joining of materials, whilst only fusing a very small volume of them [24]. It is also a fast and low-cost process with good quality control, although not ideal for highly conductive dissimilar materials [21]. Laser welding sort of solves the main issue with fastened joints, whilst raising other problems. The connection of the strips is manufactured at their edges, resulting in compact joints, and creating a solution for the non-uniform contact pressures of fastened joints [25]. The downside of laser welding is the prevalent challenge that comes with joining dissimilar materials, namely because of their different chemical, mechanical, and thermal properties [12]. Resistance spot welding's main trait is that it allows for the joining of materials, whilst only fusing a very small volume of them [24]. It is also a fast and low-cost process with good quality control, although not ideal for highly conductive dissimilar materials [21].

Recently, joining by forming techniques has emerged as an affordable, sustainable, and cost-effective option. There's been significant activity in advancing new joining processes in this field, leveraging plastic deformation to create form- and force-fit joints [26,27]. This method eliminates the need for welding, making it easy to join dissimilar materials without encountering chemical or thermal issues. However, most developed processes such as double-sided self-pierce riveting [28], injection lap riveting [29], and self-clinching [30] require the use of an additional element. For example, in self-pierce riveted joints, this typically results in an increase in the connection's weight, as the rivet is usually made of steel. Moreover, it can also raise the electrical resistance of the connection.

Recently, an innovative technique of joining by forming, known as hole hemming, has been implemented to join dissimilar materials with significantly different mechanical properties [31]. In this method, only one of the sheets undergoes plastic deformation to establish a connection, as illustrated in Fig. 1. The process involves creating a mechanical interlock between pre-punched or drilled holes through a two-stage operation: first, flanging the hole of an outer sheet, and then bending the flange over the hole of an inner sheet. Notably, this process does not necessitate additional elements or welding, which could potentially alter the thermal and electrical properties of the material sheets. Kasaei et al. [31] initially introduced, developed, and investigated joints produced through this joining process. Subsequently, the process has been successfully applied to join dissimilar materials for various applications. Examples include hole hemmed (HH) joints between aluminium (AA6082-T4) and magnesium (AZ31) [32,33], aluminium (AA6082-T4) and polycarbonate (PC) [34], as well as bonded-holed hemmed (BHH) joints between aluminium (AA6082-T4) and magnesium (AZ31) [35,36]. It is worth noting that the hole-hemmed joints produced using this technique exhibit excellent static [37,38] and fatigue performance [39], as well as superior damping properties [40].

Under these circumstances, the study aims to explore the feasibility of employing novel hole-hemmed joints in the fabrication of hybrid busbars composed of copper and aluminium with dissimilar thicknesses. The primary objective is to conduct a thermal-electrical analysis of these hybrid hole-hemmed (HHH) joints. The investigation includes a comprehensive study of the Joule heat effect in the joints through numerical simulations and experimental analysis. Additionally, the study examines the influence of temperature on the electrical resistance of the joints, considering a maximum busbar service temperature as defined by international standards for metal-clad switchgear by the IEEE [41].

In addition to this, there is an intention to understand the influence of various geometric parameters of the joint on the aforementioned analysis. In numerical simulations, several parameters are studied, including the thickness ratio of hybrid busbars t_r, hole radius R_h, and HH joint geometry, simulating the manufactured joints. Furthermore, different surface contact configurations are simulated for the HH joints. The primary aim here is to comprehend the influence of different parameters on the evolution of joint resistance with an increase in temperature. Additionally, considering that pressure significantly affects electric current flow within a joint, its impact on electrical resistance is also examined. An optimization of a new compression stage evaluated to determineits effect on the current flow from the aluminium to the copper sheet in an HH joint.

2. Hybrid busbar design

Hybrid busbar design consists of accounting for differences in electrical conductivity of the materials. The hybrid busbar representative joints were fabricated and studied bearing in mind an approximation of constant electric current flow through them. Since copper is a better conductor than aluminium, has lower electric resistivity, to maintain a constant electric current flowing through hybrid busbars, certain geometric parameters need to be accounted for. These parameters directly influence the electric potential gradient, which should be as close to uniform as possible.

The electrical conductance G of a material sheet is proportional to its cross-sectional area A, and inverse proportional to the material's electric resistivity ρ^e and length l, like Equation (1) describes:

$$G = \frac{A}{\rho^e l} \tag{1}$$

Since the single overlap joints are made from aluminium and copper sheets with the same length (l) and width (w), G is only dependent on the sheet's thickness (t) and ρ^e, therefore, the ideal cross-section area ratio for a constant electric current flow is obtained as follows:

$$A_{Al/Cu} = \frac{A_{Al}}{A_{cu}} = \frac{t_{Al}}{t_{Cu}} = \rho^e_{Al/Cu} \tag{2}$$

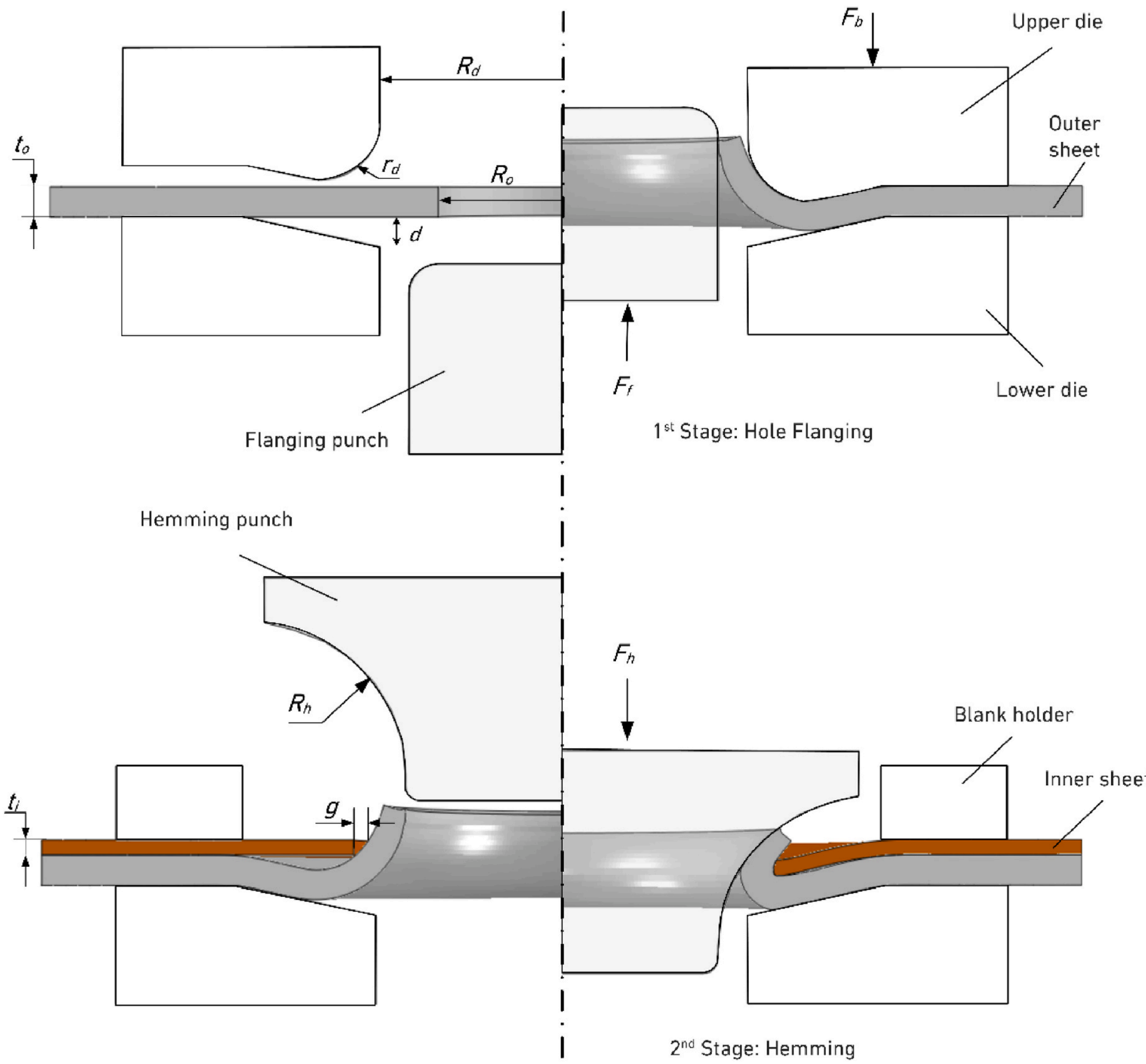

Fig. 1. Hole hemming joining technique schematic representation.

In this work, the ideal thickness ratio was calculated based on the highest material resistivity ratio obtained from the experimental thermal-electrical material characterization within the studied temperature interval of 25–105 °C (see section "5.1 Electric resistivity of the materials"). Thus, for an ambient temperature of 25 °C, given the material resistivities $\rho^e_{Al} = 3.78*10^{-8}$ Ω.m and $\rho^e_{Cu} = 1.67*10^{-8}$ Ω.m for aluminium and copper, respectively, the ideal ratio was calculated to be 2.3. The HH unit cell joints, representing hybrid busbars, were configured with a geometric condition of 2 mm for AA6082-T4 aluminium sheet thickness and 1 mm for Cu-ETP R240 copper sheet thickness, resulting in a cross-sectional area ratio of 2 (as described in Equation (2)). From a functional standpoint, this approximation closely aligns with the ideal value of 2.3.

3. Experimental procedures

3.1. Material properties

This study was conducted on AA6082-T4 aluminium and the Cu-ETP R240 copper with 2 mm and 1 mm thickness sheets, respectively. The mechanical properties of both materials were characterized by performing uniaxial tensile tests. A quasi-static condition was set in the INSTRON 3367 machine, with a test speed of 1 mm/min, performing the tests in accordance with the ASTM-E8 standard for metallic materials. Table 1 displays the mechanical properties of both materials, while Fig. 2 shows the true stress-strain curves obtained and extrapolated using the mixed Swift-Voce law for the aluminum sheet and the Swift law for the copper sheet. The thermal conductivity of the aluminium alloy and copper was considered 180 W mK [9] and 390 W mK [42], respectively.

3.2. Joining process

3.2.1. Hole hemming tool

A specially designed flexible tool [44] was used to conduct the hole hemming joining process on the aluminium and copper sheets at the Advanced Joining Processes Unit in the University of Porto/INEGI (see Fig. 3). It was mounted on an INSTRON 8801 servo hydraulic machine, where a speed of 4 mm/min was utilized to perform these experiments.

In this tool, both structural components (including upper and lower plates, guide pillars, springs, pins, bushings, flanges, keys, and nuts) and passive tool components (such as the die holder, punch holder, height adjuster, and middle plate) play vital roles. Structural components facilitate the accommodation of passive tool components, provide guidance and centring among the upper, middle, and lower plates, enable installation in the testing machine, and allow for pre-load variation of the springs. On the other hand, passive tool components

Table 1
Aluminium and copper mechanical properties.

Material	Thickness	Young's modulus (GPa)	Yield stress (MPa)	Ultimate tensile stress (MPa)	Elongation at failure (%)	Lankford coefficient, r		
						0 °	45 °	90 °
AA6082-T4 [32]	2 mm	70	173	278	24.5	0.54	0.55	0.66
Cu-ETP R240 [43]	1 mm	127	199	251	30.1	–	–	–

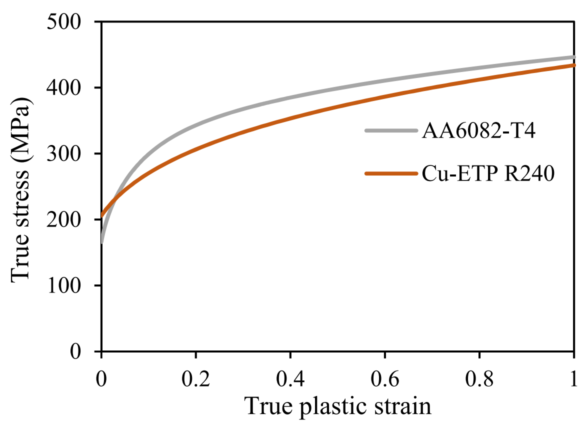

Fig. 2. True stress-plastic strain curve of the aluminium and copper sheets.

accommodate the active tool components, provide guidance and centring for them, and allow for the adjustment of their positions. On the other hand, the active tool components (i.e., dies and punches) are responsible for creating deformations on the sheets (see Fig. 4). They are interchangeable, which enables the creation of various joint geometries by easily switching them. Using different geometry punches and dies results in distinct joint geometries.

3.2.2. *Joining procedures*

The joining process comprises two separate stages: hole flanging and hemming. The first stage utilises the first set of active tools for hole flanging (Fig. 4(a)). The upper die is mounted into the die holder, while the bottom die is mounted into the middle plate. The flanging punch is then secured onto the punch holder. Once all flanging active tool components are mounted, the first stage can commence. The procedure is straightforward: the outer sheet is placed and aligned on top of the lower die, with the pins aiding in centring and aligning the outer sheet's pre-drilled hole with the flanging punch's centre axis. A fixed pre-load is applied on the springs between the lower and middle plates. As a result, when the lower plate moves upward, it pushes the springs and middle plate upward as well. Eventually, the middle plate reaches a point where it can no longer move due to contact between the lower die, outer sheet, and upper die. At this stage, the lower plate continues its upward movement, along with the punch holder and flanging punch, increasing the load applied on the springs and eventually flanging the outer sheet hole. A specific displacement is set to ensure a consistent flanging deformation for all joints.

Hemming constitutes the second and final stage of the joining

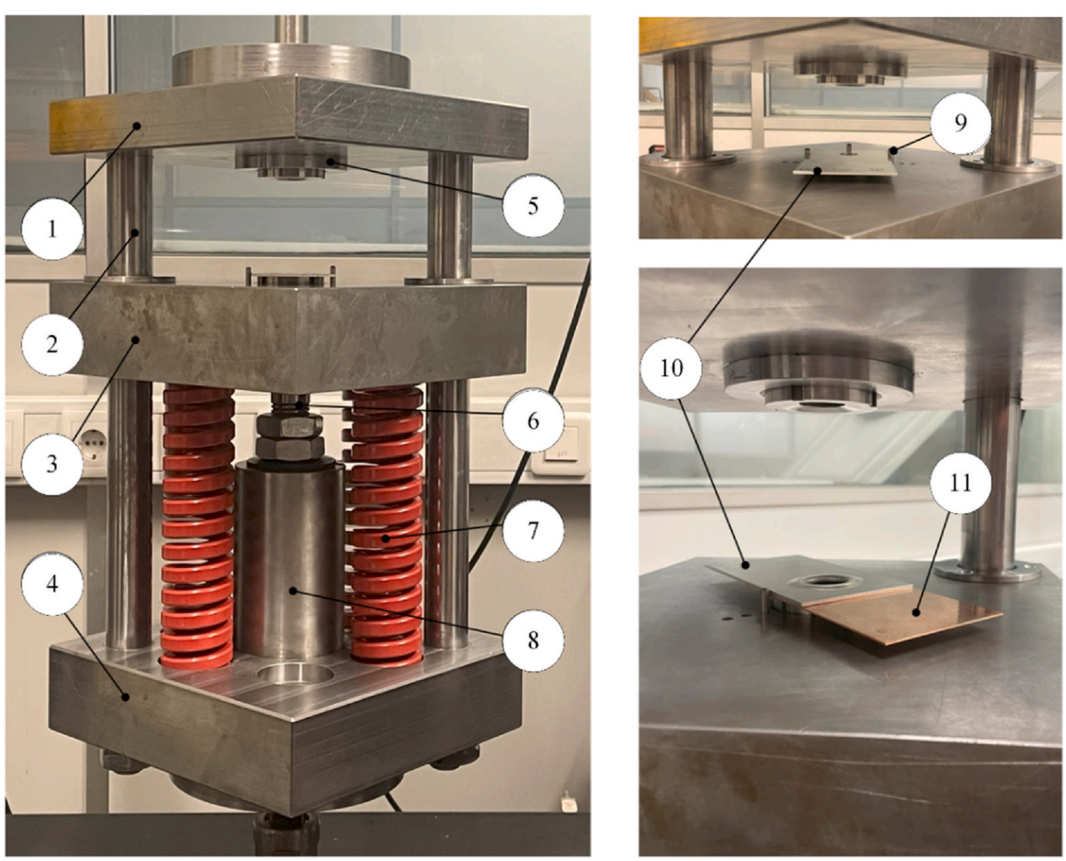

Fig. 3. Hole hemming tool components and metallic sheets: 1 - upper plate, 2 - guide pillars, 3 - middle plate, 4 - lower plate, 5 - die holder, 6 - punch holder, 7 - springs, 8 - height adjuster, 9 - pins, 10 - outer sheet (AA6082-T4 aluminium), and 11 - inner sheet (Cu-ETP R240 copper).

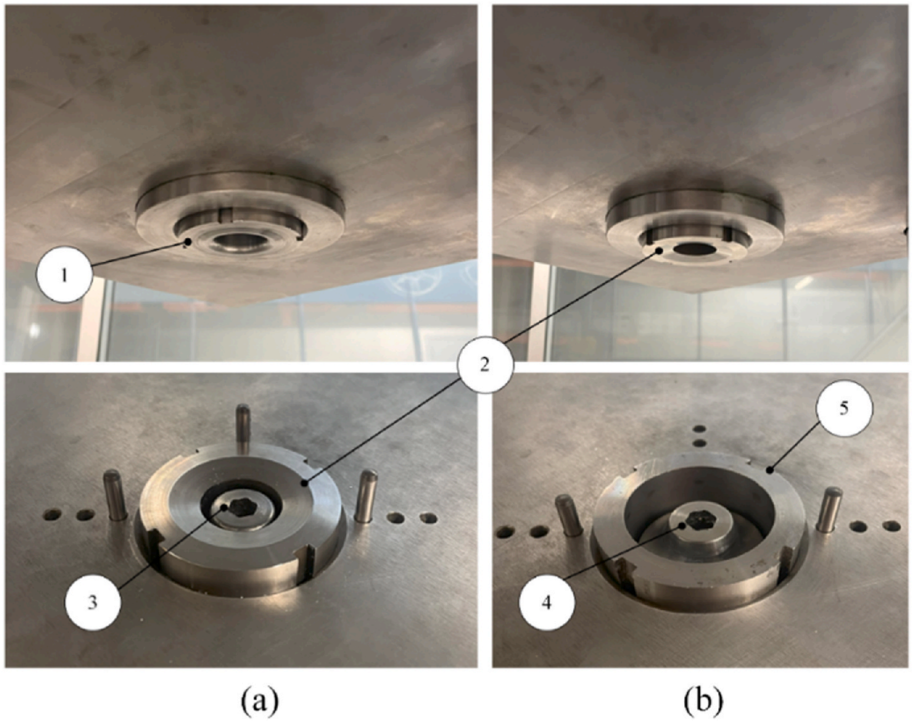

Fig. 4. Active tool components for the (a) hole flanging stage and the (b) hemming stage: 1 - upper die, 2 - lower die, 3 - flanging punch, 4 - hemming punch, 5 - blank holder.

process. Before initiating this stage, the active tool set must be changed by dismounting the hole flanging stage components and mounting the hemming stage components (Fig. 4(b)). The blank holder is then mounted onto the middle plate. The bottom die, previously mounted onto the middle plate, is now secured onto the upper plate. Additionally, the flanging punch is replaced with the hemming punch. The subsequent step involves aligning both the inner and outer sheets' holes with the centre axis of the hemming punch and placing them on top of the blank holder. The procedure for the hemming stage mirrors that of the flanging stage, albeit with different active tool set components.

Hemming the flange of the outer sheet hole onto the inner sheet hole creates a mechanical interlock. The magnitude of the mechanical interlock is directly proportional to the displacement of the hemming punch; however, it's crucial to note that excessive punch displacement can lead to fracture of the outer sheet. Thus, punch displacement must be carefully defined. The upward speed of the lower plate at 4 mm/min is also carefully regulated in both stages.

The outer sheet hole radius, R_o, the upper die radius, R_d, the fillet radius of the upper die, r_d, the indent depth, d, the fillet radius of the hemming punch R_h and the flange nominal length, F, are sensitive parameters that require careful consideration to ensure proper manufacturing of HH joints without crack propagation or unnecessary damage (refer to Fig. 1 for clarification of the parameters). The flange nominal length is a parameter dependent on R_o and R_d, as follows:

$$F = R_d - R_o \quad (3)$$

Moreover, another crucial parameter for proper joint development is the gap between the inner sheet hole edge and the outer sheet flange, g (displayed in Fig. 1), obtained as:

$$R_i = R_d + g \quad (4)$$

where R_i is the inner sheet hole radius. This parameter is crucial, as it must be sufficiently large to prevent collisions between the inner sheet and the flange.

In addition, an innovative joint configuration is fabricated, incorporating cuts in the outer sheet hole. This modification enables joint manufacturing in situations where the original simple outer sheet hole geometry (Fig. 5(a)) is not feasible due to high strains experienced at the edge of the flange. The cuts on the outer sheet hole will result in HH joints with branches. This configuration introduces additional parameters in the outer sheet hole, like the branch width, W_B, and branch length, L_B, as shown in Fig. 5(b).

The active tool components used in these experiments were selected to best fit the joint geometry requirements and were maintained at a constant configuration, as outlined in Table 2. The parameters are figuratively detailed in Fig. 1. The AA6082-T4 aluminium was chosen for the outer sheets, the Cu-ETP R240 copper for the inner sheet. The sheets were machined into 135 mm sheet length (l) and 70 mm in width (w). Table 3 displays the workplan for joint fabrication. The resulting joints are displayed in Fig. 6.

Furthermore, due to the significant influence of pressure on current flow, an additional manufacturing step was implemented for both joint configurations, with and without branches. This involved the use of a hydraulic press compression approach (Fig. 7(a)) in several joints to improve current flow. The impact of this approach on electrical resistance will be studied, and a comprehensive thermal-electrical analysis will also be conducted on these joints. For no-branch joints (Fig. 7(b)), a maximum force of 100 kN was set, while for 3-branch joints (Fig. 7(b)), a force of 60 kN was deemed optimal based on electrical resistance results (as explained in section "5.2.3 Hole hemmed joints").

3.3. *Thermal-electrical characterization*

3.3.1. *Thermal-electrical setup*

The thermal-electrical set-up used to conduct material characterization and hole hemmed joint analysis was developed at Instituto Superior Técnico in the University of Lisbon using a four-point probe technique [45]. The set-up, showcased in Fig. 8, consists of an AC transformer, the OFICEL 1.5kVA, two copper blocks that clamp the joint ends, electric cables, a KoCoS PROMET R600 micro-ohmmeter, a thermal imaging infrared camera (FLIR E86) equipped with a focal plane

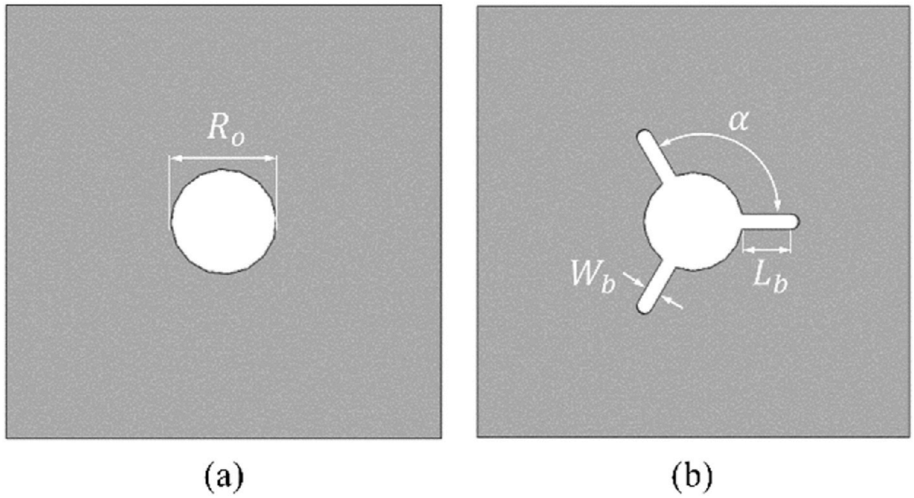

Fig. 5. Outer sheet hole radius, R_o, and 3-branch joints outer sheet hole parameters: branch width, W_b, and branch length, L_b.

Table 2
Active tool geometric parameters.

Parameter	Value (mm)
R_d	12.5
r_d	4
d	2
R_h	10

Table 3
Geometrical specifications of both the outer and inner sheets in the hole hemming experiments.

Joint type	Overlap	R_i	R_o	F	B	L_B	W_B
No-branch joint	70x70	14	8.5	4	–	–	–
3-branch joint		14.5	8	4.5	3	8	2.5

array microbolometer detector (464x348 resolution and a spectral range of 7.5–14 μm), and two voltage drop (V) measuring probes, spaced 100 mm apart.

Before the process starts, the material strips and joints were painted in black to assure the same values of emissivity, since dissimilar materials were tested. In a first heating stage, the AC transformer supplies an electric current of 1500A to the joint ends via the electric cables and, ultimately, the copper blocks, that clamp the joints. The current is supplied until a maximum temperature value of $T_{max} = 130°C$ is measured in the centre of the unit cell by the thermal camera. The point of heating the unit cells to this temperature value is to have a safety margin, because resistance measurements will be performed from $T_0 = 105°C$. This value is defined by the IEEE standard for metal-clad switchgear [41]. It represents the maximum service temperature for busbar applications.

Once T_{max} is reached, the AC transformer is switched off. The unit cells start cooling off by convection and radiation to the environment. At this point, the micro-ohmmeter KoCoS PROMET R600 is switched on and connected to the unit cell ends. Starting at $T_0 = 105°C$, an electrical current of 600A is supplied by the micro-ohmmeter for ~2s. This process is conducted several times, repeated every time the thermal camera displays a temperature drop between two consecutive measurements of $\Delta T = T_{n+1} - T_n = 5°C$, until an ambient temperature of 20 °C.

The experimental workplan for thermal-electrical analysis includes material characterization of the AA6082-T4 aluminium and Cu-ETP R240 copper, plus four HH joint configurations analysis. Table 3 displays the HH joints geometry, and the same joint configurations were used after hydraulic press compression for thermal electrical joint analysis, making a total of four distinct configurations. One material strip of each kind (aluminium and copper) was used to thermal-electrically characterize them. In order to fit the copper blocks that clamp the unit cells, both the material strips and the joints were machined to a geometry of the one showcased in Fig. 9. A total length of 150 mm, width of 70 mm with a 10 × 10 mm and 135 ° chamfer.

Fig. 6. Side-by-side joints without and with branches.

4. Finite element modelling

All finite element (FE) modelling was conducted using the ABAQUS® commercial software. Several analyses were developed, providing

(a) (b)

Fig. 7. Compression of the HH joints: (a) set-up in the hydraulic press, (b) compressed No-branch and 3-branch joints.

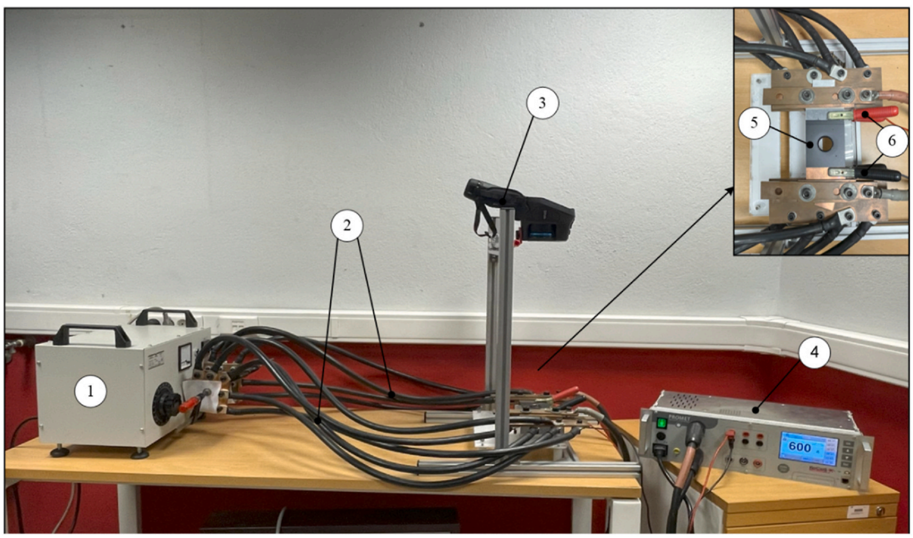

Fig. 8. Thermal-electrical analysis laboratory set-up: 1 – AC transformer (OFICEL 1.5kVA), 2 – electric current supply cables, 3 – Thermal imaging infrared camera (FLIR E86), 4 – Micro-ohmmeter (KoCoS PROMET R600), 5 – HH joint, 6 – Voltage measurement probes.

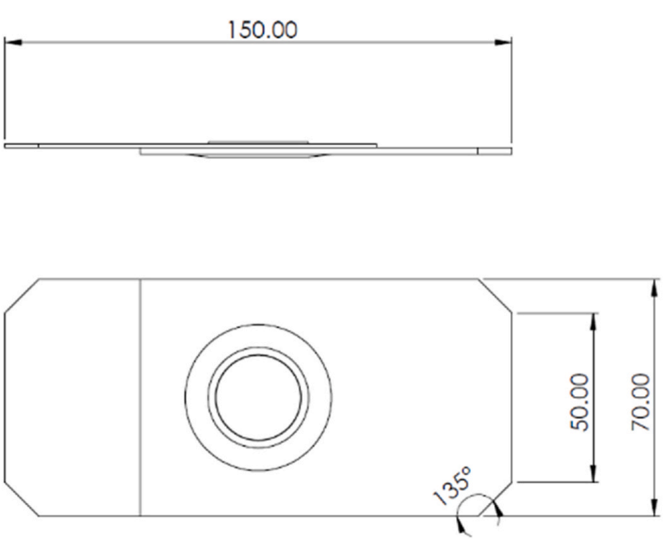

Fig. 9. Joint and material strip cuts to fit clamping on copper blocks.

different working conditions that allowed for a thorough comparison between them, and a great understanding of thickness ratio influence (t_r), hole radius influence (R), plus the actual hole hemmed (HH) joint geometry influence as well as a contact area influence on electric current flow of a busbar representative joints.

In the FE program, the governing electric field equation in a conducting material is governed by the Maxwell's equation of conservation of charge [46]. By assuming that a steady-state direct current is induced in the material, the equation reduces to:

$$\int J^* n \, dS = \int r_c \, dV \tag{5}$$

J is the electric current density (ECD), also known as current per unit area, n is the outward normal to S, which represents the surface area itself. V represents the control volume, whereas r_c is the internal volumetric current source per unit volume.

If $E(x)$ is the electrical field intensity, defined as the negative of the electric potential gradient (EPG), since φ is the electric potential, its gradient is defined as:

$$E = -\partial\varphi/_{\partial x} \tag{6}$$

Then, the flow of electric current can be described simply by the Ohm's law:

$$J = \sigma^E * E = -\sigma^E * \ \partial\varphi/_{\partial x} \tag{7}$$

In the Ohm's law, the electrical conductivity matrix is defined by $\sigma^E(\theta, f^\alpha)$, where θ is the temperature and $f^\alpha = 1, 2\ldots$ are the predefined field variables.

Finally, by use of Ohm's law in the conservation equation, written in variational form, provides governing equation of the finite element model, as it shows:

$$\int \frac{\partial \delta\varphi}{\partial x} * \sigma^{E} * \frac{\partial \varphi}{\partial x}\, dV = \int \delta\varphi J^{*} n\, dS \int \delta\varphi r_c dV \tag{8}$$

where $J \overset{def}{=} -J^{*}n$ is the current density entering the control volume, across the cross-sectional area S.

Regarding thermal energy, Joule's law describes the rate of electrical energy dissipation, denoted as P_{ec}, by current flowing through a conductor. It can be mathematically expressed as:

$$P_{ec} = J^{*}E = \frac{\partial \varphi}{\partial x} * \sigma^{E} * \frac{\partial \varphi}{\partial x} \tag{9}$$

Moreover, it is possible to define the amount of energy released as internal heat within the body resorting to the conversion factor also known as Joule heat fraction η_v multiplied by the rate of electrical energy as $\eta_v P_{ec}$. When defining this factor as unity, it converts all electrical energy into heat.

The HH joint geometry in this project was modeled based on experimental measurements and then imported into the ABAQUS® software. Fig. 10(a) illustrates an exploded view of the three modeled objects: the outer sheet (aluminium), the interface layer, and the inner sheet (copper). The thin interface layer was included to account for surface roughness, oxide films on contact surfaces, simulate different contact surface configurations between the sheets, and model applied pressure. A thickness of 0.05 mm was set for the interface layer, averaging the mechanical properties of aluminium and copper. Fig. 10(b) shows an assembled joint and how the current passes through it. The material sheets and the additional interface layer between them were modeled as 3D deformable objects and discretized using approximately 70,000 8-node linear coupled thermal-electrical elements (DC3D8E). After performing a mesh sensitivity analysis based on electric current density (ECD), temperature (TEMP), and electric potential gradient (EPG), a finer mesh with a size of 0.5 mm was applied at hole edges due to geometric complexity, while a coarser mesh with a maximum element length of 2 mm was used elsewhere (Fig. 10(c)). Additionally, four elements were assigned through the thickness of both the aluminum and copper sheets, while two elements were used for the interface layer.

Regarding its electrical resistivity, initially, an approach of averaging

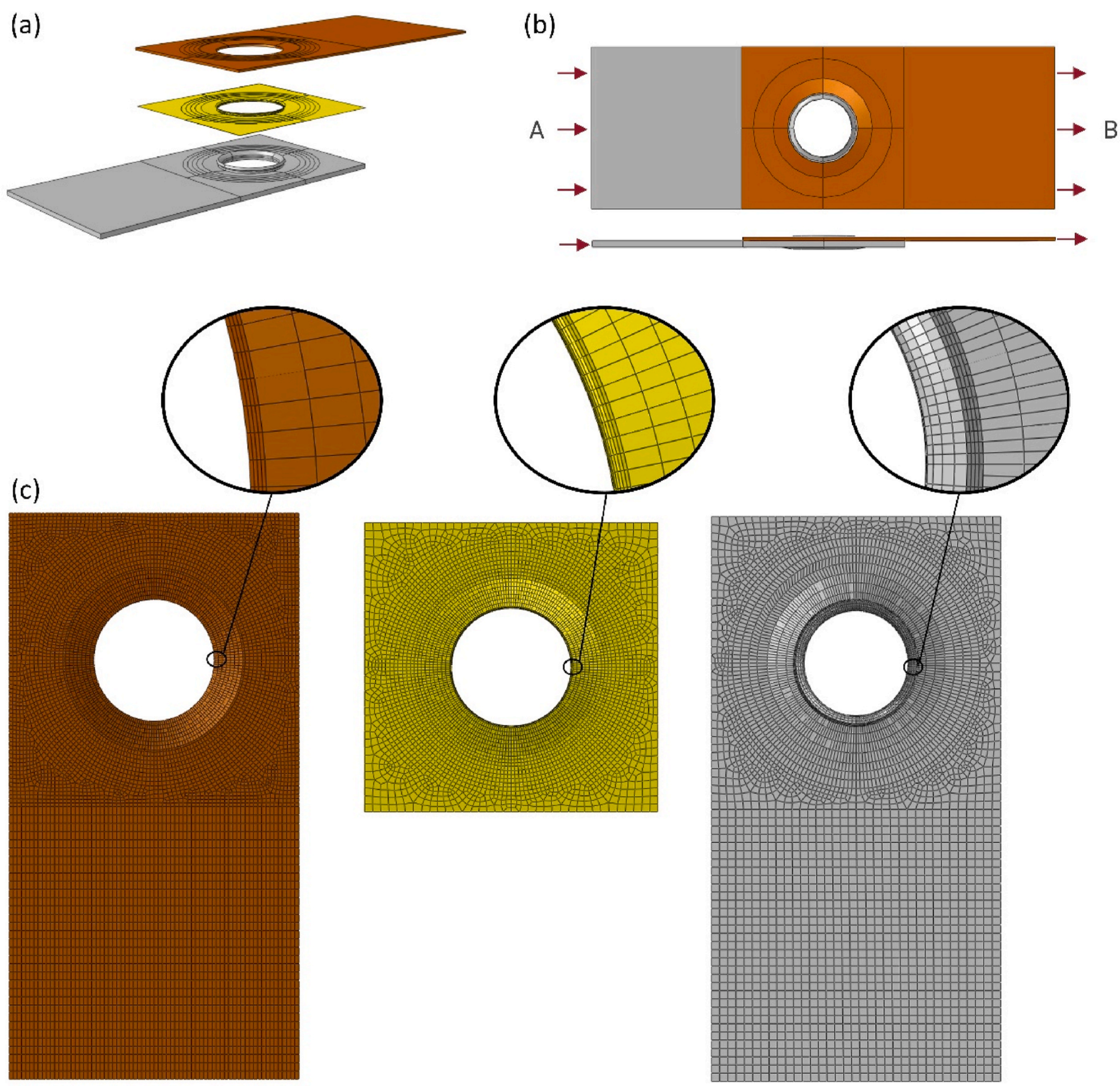

Fig. 10. Finite element model of the No-branch joint: (a) Exploded view of the copper sheet, interface layer, and aluminum sheet, (b) current flow direction, and (c) mesh details (Element type: DC3D8E, an 8-node linear coupled thermal-electrical brick element).

the resistivities of aluminium and copper was attempted. However, subsequently, a different approach was adopted, increasing the resistivity to match experimental results, aiming to simulate the oxide layer, surface roughness, and pressure between the metal sheets. It is worth noting that for simulations involving “perfect joints” and “hole joints”, the electrical conductivity properties of the interface layer were also averaged between those of aluminium and copper, as these are ideal joints modeled to study the influence of geometry.

The overall method aimed to closely approximate the experimental procedures (refer to Fig. 11). Initially, a predefined field of ambient temperature (293K or 23 °C) was applied to the joints. Subsequently, a surface current of 1500A was applied to the aluminium end surface, with a null potential boundary condition set on the opposite copper end surface, as illustrated in Fig. 10(b). Considering a cross-sectional area of 140 mm^2, a current density of 10.714 A/mm^2 was calculated and applied uniformly across the joints, mimicking the connection to the AC transformer, as conducted experimentally.

The current was maintained until the maximum busbar service temperature (T_{max}) of approximately 130 °C was reached. Subsequently, a cooldown step was initiated to allow the joint to dissipate heat to the environment through convection simulation. A heat coefficient (h) of 13 $W/(m^2K)$ was employed, as obtained from Ref. [47].

Several cooldown steps are interleaved with electric current spike steps. These spikes last for 2s and supply an electric current of 600 A, resulting in a current density of 4.286 A/mm^2, to closely simulate the experimental procedures. During these spikes, the electric potential drop (V) is measured between nodes spaced 100 mm apart, equidistant from the middle of the joints, to align with laboratory procedures. Each step is repeated 12 times to ensure sufficient data points for plotting the temperature’s influence on the joint’s electrical resistance. The boundary conditions used are listed in Table 4.

4.1. Workplan

As previously mentioned, this study involved the creation of several models. The first type consists of models designed to replicate the electrical characterization of the materials. These models help ensure that the material properties are properly defined and that the simulation accurately replicates the experimental tests. The second type consists of “perfect joint” models, which represent a single overlap joint with ideal contact conditions between the aluminum and copper sheets. The purpose of these models is to serve as a reference for comparison with more complex hole hemmed joint models. By comparing the results of the hole hemmed joint models to those of the “perfect joint” models, it is possible to assess the closeness of the hole hemmed models to the ideal reference. Additionally, the “perfect joint” models enable a straightforward study of the influence of thickness ratio (t_r), as defined in Equation (10), on the joint’s resistance, electric current flow, electric potential gradient, and Joule heat effect.

Table 4
Boundary conditions used in the thermal-electrical analysis.

Boundary condition	Heating phase	Cooldown phase
Initial Temperature Field	293K (23 °C)	–
Current Input	1500 A to the aluminum end surface	600 A to the aluminum end surface
Electric Potential	Null potential to the copper end surface	Null potential to the copper end surface

$$t_r = \frac{t_{Al}}{t_{Cu}} \tag{10}$$

It is important to note that, across all “perfect joint” models, the aluminium thickness and all ambient conditions, interactions, surface loads, and boundary conditions remained constant. Thus, the only variable that differs between these models is the thickness of the copper sheet. The values assigned to t_r include a small value of 1, indicating similar thicknesses of aluminium and copper sheets, a value of 2 (chosen for the experimental models), an ideal ratio of 2.3, and finally, a higher value of 4.

The next set of models focused on the “hole joints ", as mentioned earlier. The aim at this stage was to create several models with overlap-centered holes, each with different radius (denoted as R). Similarly to the “perfect joint” models, perfect contact conditions were set for these models, given the aim rellying on a geometry’s influence study on current and resistance. Initially, a hole with an 8.5 mm radius was modeled, corresponding to the outer sheet (aluminum) hole radius R_o of the No-branch joint. Subsequently, the radius of the manufactured joints after hole hemming was measured at approximately 11.85 mm. Thus, a hole joint with $R = 11.85$ mm was modeled. Finally, mirroring the first hole model, a joint with $R = 14.5$ mm was modeled to represent the inner sheet radius, R_i, for the branch-less joints.

Finally, thermal-electrical analysis was conducted on two types of HH joints: No-branch and 3-branch ($B = 3$) joints. Comparing these models provides insight into the influence of HH joint geometry, including the impact of branches on electrical resistance. Furthermore, both pre-compressed and post-compressed joints were modeled and studied to elucidate the influence of the compression stage. Table 5

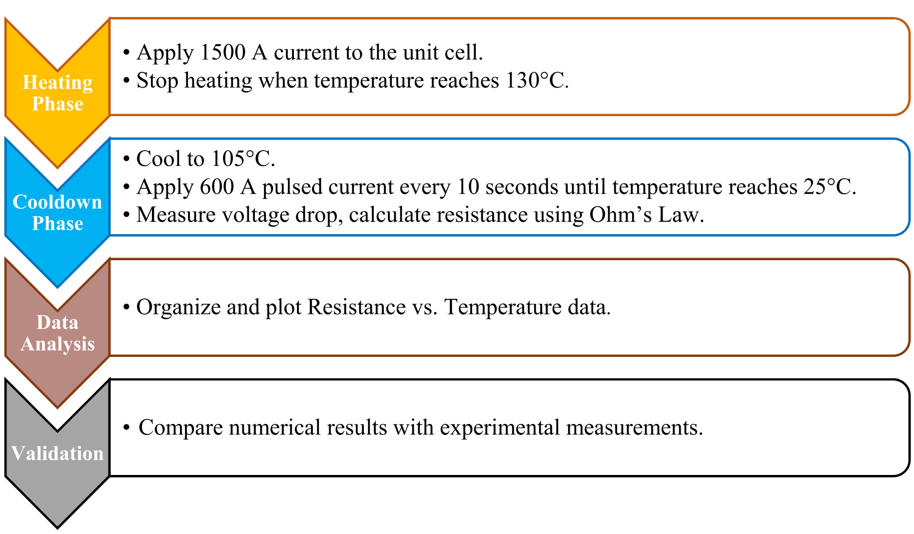

Fig. 11. Thermal-electrical analysis process.

provides an overview of the various models developed in the finite element software.

In the analysis of experimentally manufactured joints, it was observed that the contact between the aluminium and copper sheets is not perfect. As a result, contact interactions in FE models representing pre-compressed and post-compressed joints differ from each other, as shown in Fig. 12. A noticeable increase in contact was observed in the HH joints after the application of compression by the hydraulic press. This increase occurred both in the overlap and in the flange area.

In joints manufactured with three branches, contact was not observed in the middle area of the branches. Therefore, in the flange area, only the corners of the branches were taken into account. Initially, the hydraulic press compresses the flange onto the inner sheet hole edge, subsequently bending the copper sheet, which then contacts the aluminium outer sheet around the flange area. This contact was not present before compression, which explains why the crown area around the flange was not considered in pre-compression joints. Furthermore, no contact was assumed in the overlap area around the outside of the largest partition circle. This observation was confirmed through gap mapping of the manufactured HH joints, which revealed no contact up to the mentioned partition circle. It is worth noting that different partitions were employed in branchless joints and those with branches, reflecting various contact configurations tested by the authors to accurately approximate finite element models to experimental joints. This approach allowed for a comprehensive exploration of contact interactions in the joints.

5. Results and discussion

5.1. Electric resistivity of the materials and model verification

Fig. 13 presents the results of the thermal-electrical material characterization for AA6082-T4 aluminum and Cu-ETP R240 copper, obtained directly from experimental tests, along with the numerical results. Observing Fig. 13, it becomes evident that an increase in temperature significantly influences the electrical resistivity of the material, showing an approximately linear relationship. Furthermore, the excellent agreement between the numerical and experimental results, with an error of less than 1 %, confirms that the developed model accurately replicates the experimental data.

5.2. Electric resistance of the hybrid busbars

5.2.1. Influence of thickness ratio

The first geometry parameter that was studied regards the thickness of both material strips. This study was conducted to better understand how electric current density (ECD), temperature (TEMP) and electric potential gradient (EPG) are influenced by different copper sheet thicknesses, for a constant aluminium thickness of 2 mm (Fig. 14). Moreover, the electric resistance of these joints was also obtained. The thickness ratio, t_r, explained in the workplan on the "4 Finite element modelling" section, is a ratio between the thicknesses of the aluminium and copper strips. Essentially, four different thickness ratio "perfect joint" models were simulated and compared between one another.

Table 5
Geometrical parameters of the joints for FE thermal-electrical simulations.

Models	Parameter (s)	Value (mm)			
Perfect joints	t_r	1	2	2.3	4
Hole joints	R	8.5	11.85	14	
Hole hemmed joints (pre- and post-compression)	F	4			
	R_o	8.5			
	R_i	14			
	B	0	3		
	L_b	8			
	W_b	2.5			

Fig. 14(a) illustrates the temperature contours for the four simulated "perfect joint" models. It is evident that for $t_r = 4.0$, corresponding to a 2 mm aluminium sheet and a 0.5 mm copper sheet, the highest temperature is reached on the copper sheet, specifically on the right-hand side. In contrast, for $t_r = 2.0$, the temperature contours show approximately equal maximum temperatures for both sheets. The displayed contour represents a specific time increment where the maximum joint temperature reaches 378K (105 °C). At this temperature, the ratio between the electric resistivity of the materials (shown in Fig. 14(d)) is calculated as $\frac{1}{\frac{\rho^e_{Al}}{\rho^e_{Cu}}} = \frac{1}{\rho^e_{Al/Cu}} = \frac{1}{\frac{46.88}{21.60}} = 0.46$, which precisely matches the thermal conductivity ratio between both materials: $\frac{k_{Al}}{k_{Cu}} = k_{Al/Cu} = \frac{180}{390} = 0.46$. It's worth noting that the thermal conductivity values for copper [42] and aluminium [9] were obtained from literature sources and are displayed in Table 1.

The Wiedemann–Franz law provides an explanation for the relationship between thermal and electrical conductivity.

$$\frac{k}{\sigma} = LT \tag{11}$$

where k is the thermal conductivity, σ is the electrical conductivity of a material, L is the Lorentz number, and T is the temperature. As noted before, resistivity is given by the inverse of conductivity:

$$\sigma = \frac{1}{\rho^e} \tag{12}$$

It is possible to account for the actual resistance of the material strips, because the sheets have different thicknesses:

$$\rho^e = \frac{RA}{l} \tag{13}$$

where R is the electrical resistance, A the cross-section area, and l is the length of the strip material. Now, substituting the electrical conductivity, σ, in Equation (11) by resistivity as in Equations (12) and (13), it is obtained:

$$k\frac{RA}{l} = LT \tag{14}$$

If a ratio is created between aluminium and copper regarding this equation, bearing in mind that in most metals, the Wiedemann-Franz-Lorenz law is well evidenced at close to ambient or slightly elevated temperatures [48], it is obtained:

$$\frac{k_{Al}\frac{R_{Al}A_{Al}}{l_{Al}}}{k_{Cu}\frac{R_{Cu}A_{Cu}}{l_{Cu}}} = \frac{L_{Al}T_{Al}}{L_{Cu}T_{Cu}} = k_{Al/Cu}\frac{R_{Al/Cu}A_{Al/Cu}}{l_{Al/Cu}} = L_{Al/Cu}T_{Al/Cu} \tag{15}$$

Respective resistance of the aluminium and copper 2 mm and 1 mm sheets was obtained at 105 °C (378K) during material thermal-electrical characterization as $R_{Al_{378K}} = 32.67\mu\Omega$ and $R_{Cu_{378K}} = 30.55\mu\Omega$. The length, l, of the aluminium and copper sheets is the same, as mentioned in previous sections, therefore its ratio is $\frac{l_{Al}}{l_{Cu}} = 1$. Moreover, since the width, w, of the material strips is also the same, simplifying by additionally taking into account the thickness ratio, t_r (Equation (10)), the ratio of the cross-sectional area resumes to:

$$A_{Al/Cu} = \frac{A_{Al}}{A_{cu}} = t_r \tag{16}$$

Thermal conductivity ratio was aforementioned calculated and temperature, T, at the time (increment) of analysis is 378K, also previously mentioned. The Lorentz number, at ambient or slightly elevated temperatures is around $L_{Al} = 2.1*10^{-8}$ WΩK^{-2} and $L_{Cu} = 2.54*10^{-8}$ WΩK^{-2} for aluminium and copper, respectively [48]. However, because the authors assumed constant thermal conductivity values for

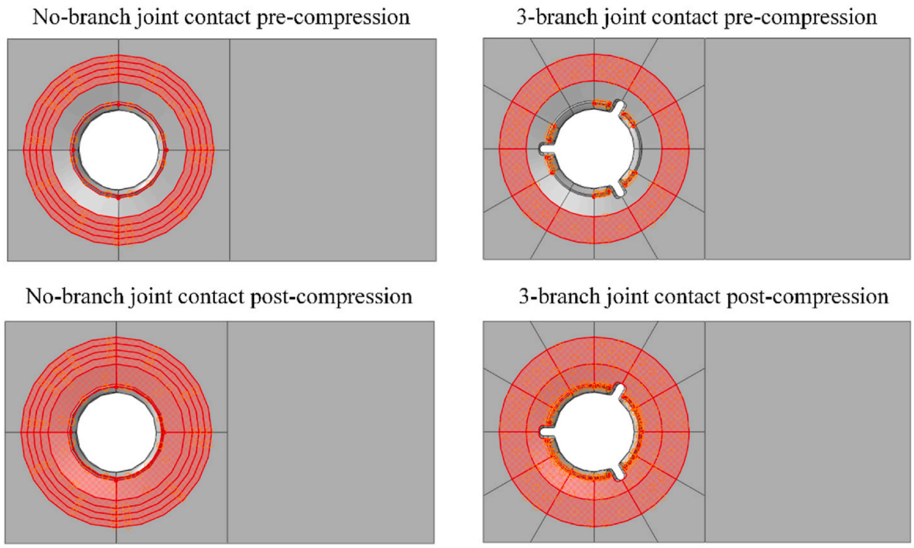

Fig. 12. Contact interactions for the various pre- and post-compression No- and 3-branch joint models.

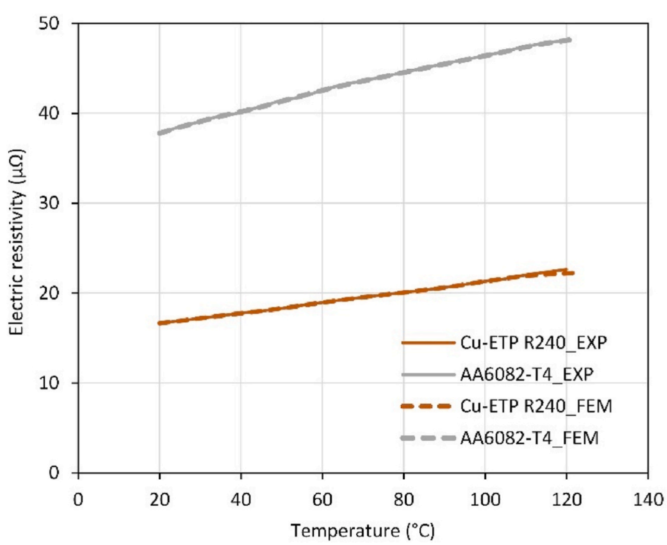

Fig. 13. Comparison of numerical and experimental evolution of electrical resistivity with temperature for AA6082-T4 aluminum and Cu-ETP R240 copper.

both materials, given that it does not affect, neither englobes the main aim of this study, the assumed-close to theoretical value for the Lorentz number for both materials is obtained from the Wiedemann–Franz law as:

$$\begin{cases} L_{Al_{378K}} = \dfrac{k_{Al}}{\sigma_{Al_{378K}} T} = \dfrac{180}{21330398.27*378} = 2.23 \ \ *10^{-8} \ \mathrm{W\Omega K^{-2}} \\ L_{Cu_{378K}} = \dfrac{k_{Cu}}{\sigma_{Cu_{378K}} T} = \dfrac{390}{46298761.28*378} = 2.23 \ \ *10^{-8} \ \mathrm{W\Omega K^{-2}} \end{cases} \tag{17–18}$$

Finally, at a temperature of $T = 105^{\circ}C$ (378K) and accounting for all the abovementioned factors, it is possible to re-write Equation (15) in order of thickness ratio, t_r:

$$t_r = \frac{L_{Al/Cu} T_{Al/Cu} l_{Al/Cu}}{k_{Al/Cu} R_{Al/Cu}} = \frac{\dfrac{2.23*10^{-8}}{2.23*10^{-8}} * \dfrac{378}{378} * 1}{0.46 * \dfrac{32.67}{30.55}} = 2.03 \tag{19}$$

To conclude temperature contour analysis, this value essentially represents the thickness ratio to which at a temperature of $T = 105^{\circ}C$ (378K), the copper and aluminium sheets would reach exactly the same temperature. Therefore, it justifies why a thickness ratio of $t_r = 2.0$ presents such close temperature contour and maximum values between the aluminium and copper sheets. A thickness ratio of $t_r = 1$ (Fig. 14(a)) showcases much higher temperature reach in aluminium, as expected because of thermal conductivity properties, for the earlier stated reasons.

Regarding electrical current density (ECD), equal results in copper and aluminium are obtained for a thickness ratio of $t_r = 1.0$ (Fig. 14(b)). In the joint overlap, because perfect contact conditions were set, ECD is not as high as further away from it, given that the current in that area is flowing through a total of 3.05 mm (2 mm aluminium thickness, 1 mm copper thickness plus 0.05 mm thin interface layer thickness) thickness material. Away from the joint overlap, the total material thickness is 2 mm, therefore showing lower ECD values. This is transversal to the other t_r models, explaining why in $t_r = 2.3$ and $t_r = 2.0$ ECD is higher in copper, and much higher for $t_r = 4.0$. A value of ECD $= 1.07143 * 10^7 \mathrm{A/mm^2}$ is observed for all models in the aluminium sheet, which is expected since its thickness was kept constant (2 mm) and it represents the exact value of surface current that was input in the analysis, validating a proper current flow through the materials.

Finally, regarding the electric potential gradient (EPG) (Fig. 14(c)), as Equation (7) suggests, its negative (Electric field intensity, E (x)) multiplied by the electric conductivity matrix, σ^E, gives the electrical current density, J, which written in a ratio manner between the aluminium and copper sheets comes as:

$$J_{Al/Cu} = -\sigma^E{}_{Al/Cu} * \partial\varphi / \partial x_{Al/Cu} \tag{20}$$

Writing this equation with regards to the electric potential gradient, for a thickness ratio of $t_r = 2.3$, exporting the values from the ECD results (Fig. 14(b)) and knowing the conductivity matrix solely depends on temperature, for $T = 378\mathrm{K}$:

$$\left(\partial\varphi / \partial x_{Al/Cu}\right)_{378K} = \left(\frac{J_{Al/Cu}}{-\sigma^E{}_{Al/Cu}}\right)_{378K} = \left(\frac{\dfrac{J_{Al}}{J_{Cu}}}{-\sigma^E{}_{Al} / -\sigma^E{}_{Cu}}\right)_{378K} = \frac{1.07143*10^7 / 2.46587*10^7}{(-21330398.27)/(-46298761.28)} = 0.94 \tag{21}$$

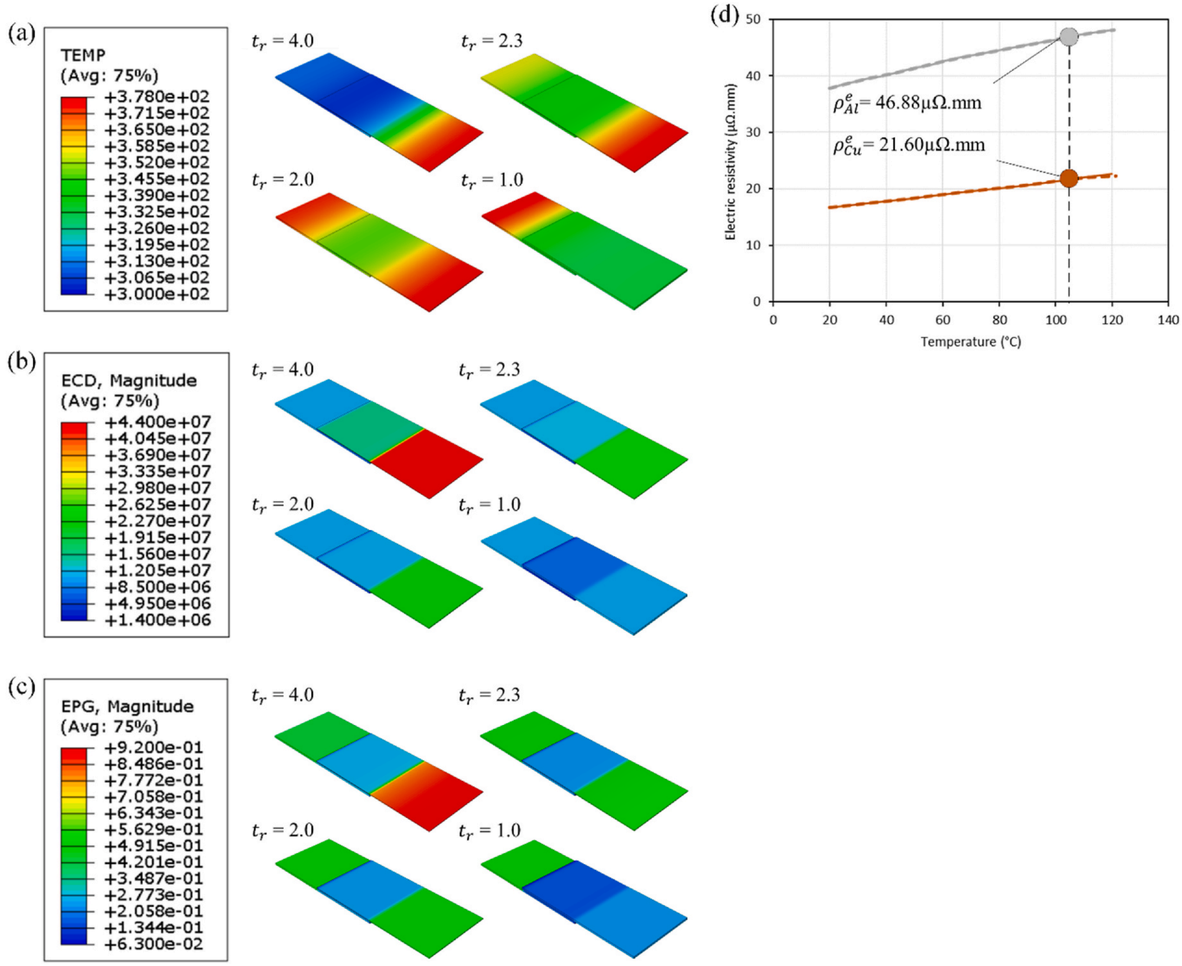

Fig. 14. Thickness ratio, t_r, influence on "perfect joint" models at $T = 105^{\circ}C$ during the heating stage by Joule effect on: (a) temperature (TEMP) contour $[K]$, (b) electric current density (ECD) $[\frac{A}{m^2}]$, (c) electric potential gradient (EPG), and (d) temperature's influence on electric resistivity of the materials. Note: AA6082-T4 aluminium is the left-hand side material sheet and Cu-ETP R240 copper is the right-hand side material sheet, across all models.

This value represents the ratio between the electric potential gradient from the aluminium sheet to the copper sheet, suggesting that for an ideal thickness ratio of $t_r = 2.3$, for a temperature of $T = 378$K, the aluminium sheet EPG has a value of 0.94 times that of copper, explaining the similarities in contour (Fig. 14(c)). Applying this idea across the other models, it is understandable why for $t_r = 4$ a much larger potential gradient is obtained in copper than in aluminium, given that the conductivity matrix (σ^E) ratio is the same, ranging from 2.27 at ambient temperature to 2.17 at 378K, and the ECD in copper is 4 times higher, for the same current is flowing through ¼ of the cross-section when compared to aluminium. It justifies why EPG in copper is roughly $4/2.17 = 1.84$ times higher than in aluminium. A $t_r = 1$ shows how roughly 2.17 times higher EPG values are obtained in aluminium (for the same reasons as for the other models) and $t_r = 2$, representing the actual thickness ratio used in experimental procedures, shows an almost constant electrical potential gradient across the material sheets. Given that Equation (7) introduces the flow of electrical current described simply by the Ohm's law, this fundamentally suggests that the premise of the selection of material thicknesses, explained in the "2 Hybrid busbar design" section, is showcasing an approximately equal current flow throughout the joint.

Finally, Fig. 15(a) showcases the electric potential (EPOT) drop (V) with the highlighted 100 mm spaced measurement nodes. To recall, the electric potential drop (V) (EPOT) measurement between the aforementioned nodes, then, by the Ohms law, divided by the input electric current, gives the resistance of the joint, showcased in Fig. 15(b) for the various t_r models, to best simulate the experimental conditions under which the manufactured unit cells were tested. A direct relationship between thickness ratio and increased resistance is observed, given that an increase in t_r means a smaller thickness for the copper sheet, meaning less material for the electric current to flow through. The EPOT contour results show how for smaller thickness ratios the electric potential in the aluminium and copper sheets get closer to one another, meaning a lower potential drop is observed between them, therefore presenting lower electrical resistance. This phenomenon is observed across an increase in temperature as well (Fig. 15(b)).

5.2.2. *Influence of hole radius*

As outlined in the "4.1 Workplan" of the "4 Finite element modelling" section, three models featuring cantered and perfectly aligned holes were simulated (see Fig. 16). The thickness ratio was set to $t_r = 2$ based on the premise of maintaining constant current flow, as explained in previous sections. Due to the extremely similar results obtained, only the outcomes of simulations featuring outer and inner sheet hole radii of $R = 8.5$ mm and $R = 14$ mm, respectively, will be presented. These results were compared with the $t_r = 2$ model to assess the sole influence of including a hole on both sheets.

Fig. 16(a) illustrates the impact of hole inclusion on temperature contours at a specific increment, where the joint reaches a maximum temperature of 378K (105 °C), as previously analysed for t_r influence. While the inclusion of the hole does affect the time it takes for the joint to reach elevated temperatures—reducing it due to a cylindrical lack of

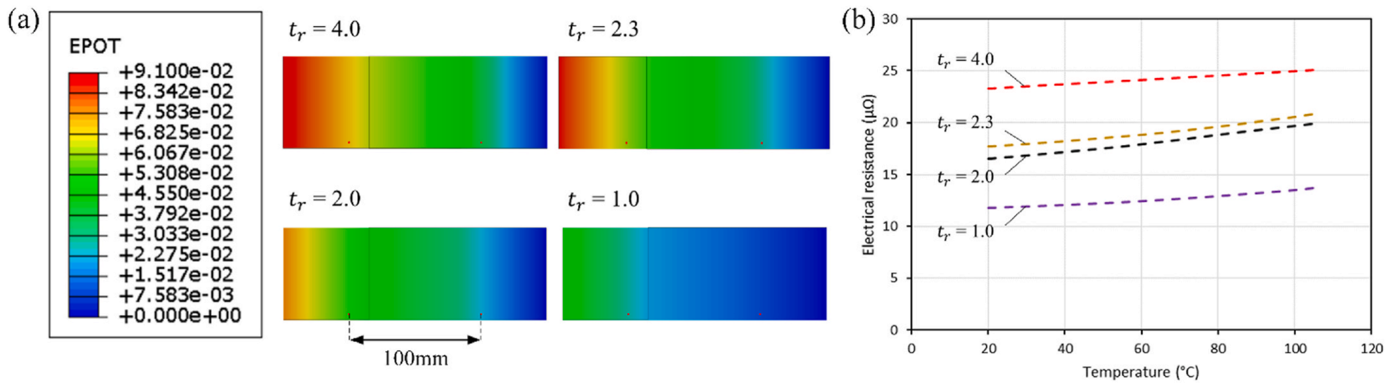

Fig. 15. (a) Electrical potential $[V]$ results for different thickness ratio, t_r, "perfect joint" models at ambient temperature ($T = 20°C$) in the initial heating stage by Joule effect and (b) temperature's influence on electrical resistance "perfect joint" models. Note: AA6082-T4 aluminium is the left-hand side material sheet and Cu-ETP R240 copper is the right-hand side material sheet, across all models.

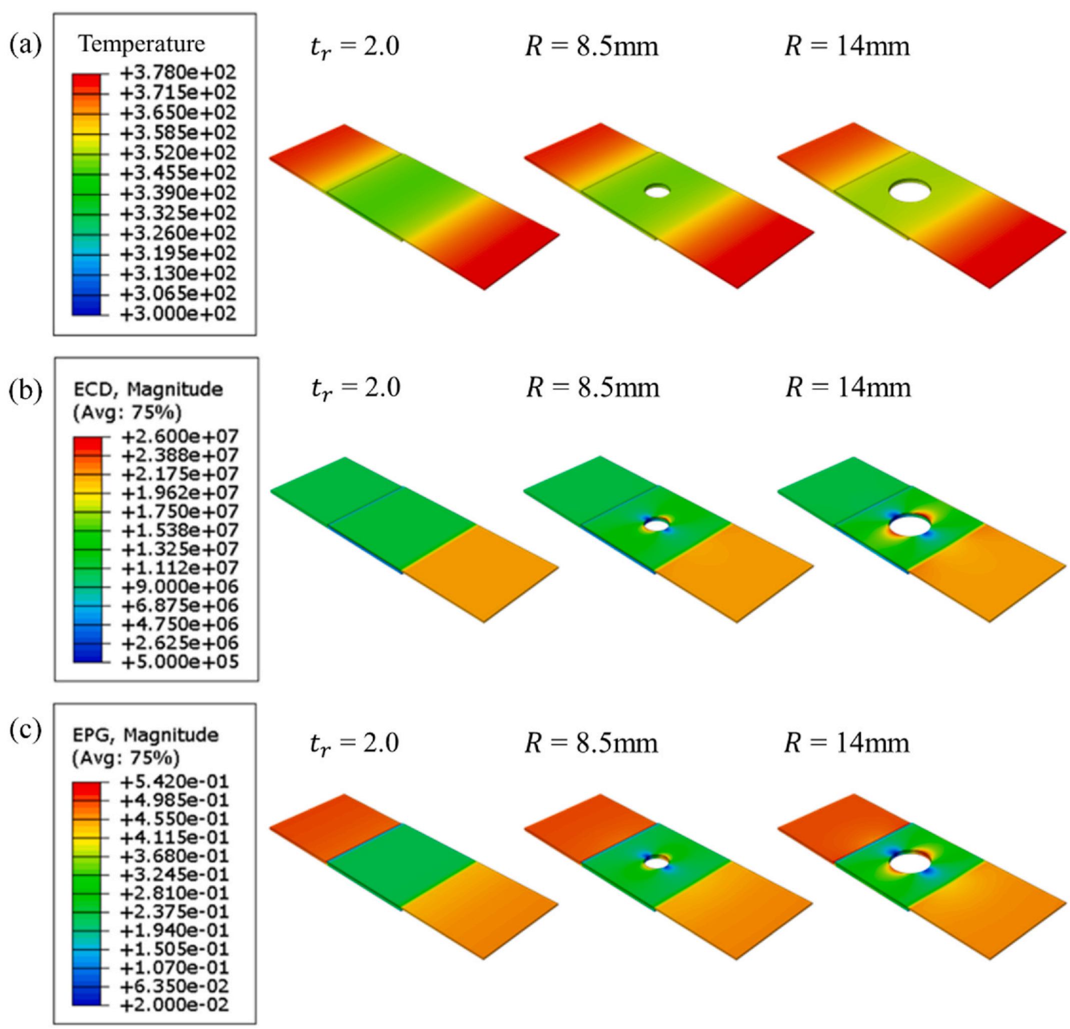

Fig. 16. Hole radius, R, influence on "hole joint" models at T = 105 °C during the heating stage by Joule effect on: (a) temperature contour, (b) electric current density $[A/mm^2]$, and (c) electric potential gradient. Note: AA6082-T4 aluminium is the left-hand side material sheet and Cu-ETP R240 copper is the right-hand side material sheet, across all models.

material at the joint's centre—it does not significantly alter the temperature distribution across the joint, as suggested by Fig. 16(a).

This lack of significant alteration is attributed to the consistent overlap conditions and interactions, which remain unchanged from previous simulations, resulting in no discernible effect on temperature distribution. However, heat dissipation does occur around the hole in the joint's centre. In perfect joints without holes, heat dissipation primarily occurs across the top and bottom surfaces of the cylindrical area represented by the hole. In contrast, with hole inclusion, heat is dissipated around the cylinder wall surrounding the hole, as there is no material present on the top and bottom surfaces in these conditions. This nuanced difference also explains why joints with holes reach elevated temperatures more quickly and why the temperature contour remains unchanged. Heat dissipation through convection occurs similarly around the hole, along the cylinder walls.

Fig. 16(b) and (c) depict the contours for electrical current density (ECD) and electrical potential gradient (EPG), respectively. It was observed that the inclusion of the hole significantly influences their distribution, as current is compelled to flow around the hole, disrupting the continuous and constant path observed in ideal joints. Given that the electric potential gradient is defined as $\partial\varphi/_{\partial x}$, around the hole the EPG reaches its maximum value on the side wall of the cylinder, at $\theta = \pm 90^\circ$, and its minimum values are obtained at $\theta = 0^\circ$ and $\theta = 180^\circ$, because of impediment of flow due to the lack of material that the electrically charged particles face (see Fig. 17 for clarification of the θ parameter).

Regarding ECD (Fig. 16(b)), because the current density is obtained as a function of the electric potential gradient and the conductivity matrix, σ^E (see Equation (7)), since the aforementioned matrix is solely dependent on temperature, for a constant T, ECD behaves like the EPG, $\partial\varphi/_{\partial x}$. This explains why its contour is similar to EPG, factored by σ^E.

The electric potential (EPOT) contour results of the "hole joints" are displayed in Fig. 18(a), alongside the obtained electrical resistance for this type of joints (Fig. 18(b)), with an extra reference model: $t_r = 2$. The results are quite clear, with an increase in resistance directly related to an increase in hole radius, R, expectedly. The EPOT contour of the various hole joints explains the increase in resistance. The results are quite close given that the inclusion of holes simply impacts resistance because a lack of material is now present in the centre of the joint.

5.2.3. *Hole hemmed joints*

Fig. 19 presents a comparison of the temperature contour, at $T_{max} = 105\ ^\circ C$, at a certain time of the analysis when the mentioned maximum temperature is obtained at the centre of the unit cell. Fig. 19(a) presents the experimentally recorded temperature by the thermal imaging infrared camera and Fig. 19(b) displays the numerically obtained results when the joint with branches pre-compression model reaches this temperature. By observation it is clear that a good agreement was obtained between FE models and the thermal-electrical experiments, although because of different pressures around the flange area of the outer sheet, there are some "hot-spots" captured by the thermal camera. It was expected because of small deviations in contact pressure distribution around the flanges, given that the higher the pressure the better the current will flow through.

Fig. 20(a) and (b) show the results for the thermal-electrical analysis of joints without and with branches before applied compression, respectively. Branch-less joints presented a more or less constant electrical resistance throughout the experiment in temperature decreasing resistance measurement. This is because thermal expansion played an impactful role throughout the analysis. Because of initially poor contact between the material sheets, and low levels of pressure being applied by the outer sheet flange around the inner sheet hole edge, there was room for oxide layer to form between the sheets, given that small gaps exist between them. Furthermore, the electrical resistance is not linearly increasing with temperature because of thermal expansion. The small gaps that exist at lower temperatures are non-existent at higher temperatures, given that with temperature increase the materials expand creating contact between the sheets that once, at low temperatures, did not exist, explaining the variable results of electrical resistance with temperature increase.

The elimination of gaps upon compression generates small pressure at the new aluminium-copper sheet contact points. This contributes to lowering resistance: pressure positively impacts current flow. As temperature increases, the gap filling process becomes less significant, stabilizing pressure and contact conditions. At this point, the increase in electrical resistance is primarily due to temperature elevation. Initially, 3-branch unit cells (pre-compression) exhibited minimal pressure and lacked rotation constraints around the centre of the hole, allowing sheets to rotate freely. Consequently, significant oxide layers, poor contact, and low pressure were evident between the sheets, leading to high electrical resistance. Thermal expansion played a crucial role in breaking oxide layers and increasing sheet contact, particularly in 3-branch joints due to their initial state.

It's worth noting that the interface layer properties were instrumental in simulating oxide layers between the sheets and modelling thermal expansion. The interface layer's conductivity properties varied with temperature to match experimental results, opposite to the materials' behaviour. In the No-branch pre-compression simulation, the interface layer exhibited conductivity properties that varied with temperature to closely replicate experimental conditions.

A comprehensive investigation into the influence of pressure on the electrical resistance of the joints was undertaken. Fig. 20(c) illustrates the impact of pressure on the joint's electrical resistance at a constant ambient temperature. This data was obtained through successive hydraulic press compression stages of 20 kN, 40 kN, 60 kN, and 100 kN. The experimental procedure involved subjecting the joints to compression at a constant moving speed of 5 mm/min at each specified pressure level, followed by measuring electrical resistance at room temperature. For branchless joints, the results demonstrated a linear decrease in resistance with increasing pressure, as depicted in Fig. 20(c). Consequently, a hydraulic press compression of 100 kN was selected for joint thermal-electrical testing, as it yielded the lowest resistance. In contrast, joints with three branches exhibited a different response to pressure. Beyond a compression force of 60 kN, the resistance began to increase (Fig. 20(c)). Therefore, 60 kN hydraulic press compression was deemed optimal for the thermal-electrical analysis of 3-branch post-compression

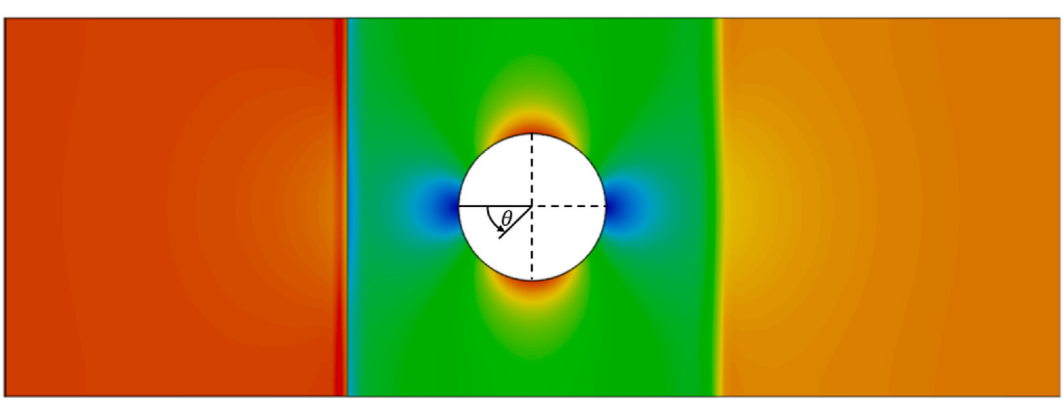

Fig. 17. Introduction of θ parameter in "hole joints" representing the angle to which the current flows around the centered hole in the joint (electric potential gradient, EPG, contour).

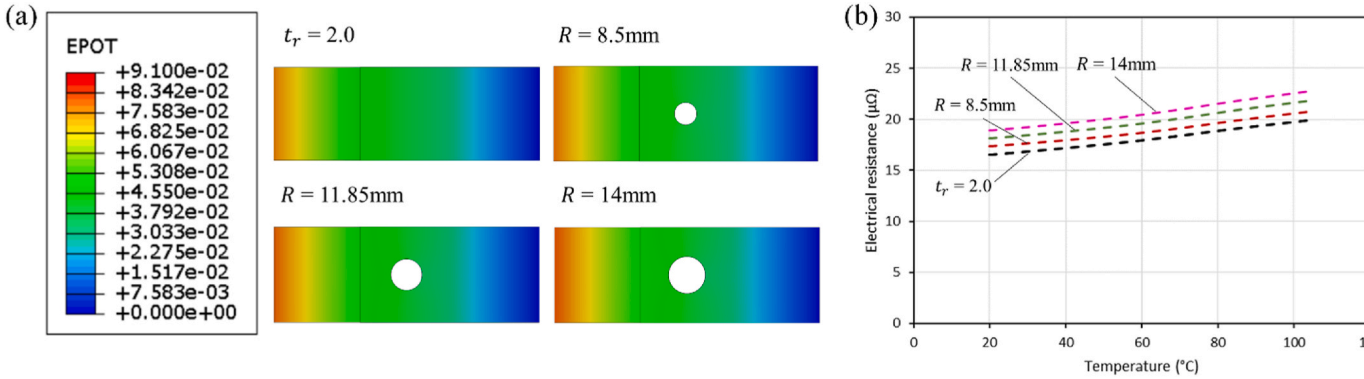

Fig. 18. (a) Electrical potential (V) results for different hole radius, R, “hole joint” models at ambient temperature ($T = 20^{\circ}C$) in the initial heating stage by Joule effect and (b) temperature’s influence on electrical resistance on “hole joint” models. Note: AA6082-T4 aluminium is the left-hand side material sheet and Cu-ETP R240 copper is the right-hand side material sheet, across all models.

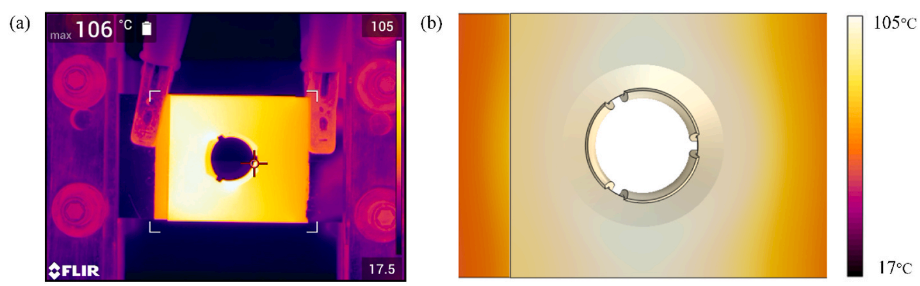

Fig. 19. Temperature distribution for an instant of analysis time corresponding to a maximum temperature on the centre of the unit cell of $T_{max} = 105^{\circ}C$ for HH pre-compressed joints with branches: (a) experimentally obtained by the thermal imaging infrared camera, and (b) numerically predicted by the finite element simulations.

joints.

Fig. 20(d) and (e) show the joints electrical resistance-temperature results after compression. It’s clear that the hydraulic press compression had a very positive impact on current flow of the joints. Thermal expansion no longer significantly impacts the contact between the sheets, given that high pressure is now present in the joint overlap. Expectedly, due to higher pressure and larger contact area (in the bearing area of the joint, given no cuts are induced in the outer sheet machining), the post-compression branchless joints showcase lower electrical resistance at any temperature than 3-branch post-compression joints, with a 29.51–36.07 μΩ and 35.80–42.13 μΩ interval, respectively, for a temperature interval of 25–105 $^{\circ}C$. It is worth noting that the comparison between experimental and numerical results confirmed the validity of the finite element models created for the joints with different configurations and pre- and post-compression conditions, with an error of less than 5 %.

Regarding electric current density $[\frac{A}{m^2}]$, the results are quite similar across the No-branch and 3-branch models before and after compression (Fig. 21). This is because current flow is mainly done through overlap contact between the material sheets, given that the flange contact area around the bearing area is quite small, and has a very small impact on the current flow (tested in solely flange area contact models). From pre-compressed to post-compressed joint models the biggest impact on current flow is due to the added circular area of contact surrounding the flange (check Fig. 12 for clarification). This improves current flow, and a slightly more uniform distribution of ECD can be observed in these models, especially in the copper sheet area closer to the flange area. Regarding the highest ECD areas, a similar behaviour to “hole joints” is observed, with current flowing around the bearing area because of geometric impediment of the aforementioned, reaching the highest values at approximately $\theta = \pm 90^{\circ}$ (check Fig. 17 for θ parameter clarification).

5.3. Shear tests

Pre- and post-compression joints underwent shear tests at room temperature in order to evaluate their mechanical performance (Fig. 22). Fig. 22(a) shows the shear test force-displacement curves for both pre- and post-compressed No- and 3-branch joints. Initially, there is a rapid increase in load attributed to the elastic deformation of the material sheets. Subsequently, significant bending of the copper sheet occurs, leading to deformation of its hole against the flange. This results in a further increase in load for all joints, except for the pre-compressed No-branch joint, which stabilizes at a constant load. This stabilization occurs because of the increasing contact between the inner sheet hole edge and the outer sheet flange. Following compression, the flange exerts downward pressure on the outer sheet around its hole area, reducing the bearing area that restricts movement of the copper sheet in a shear load configuration. Consequently, compressed joints sustain lower displacements and loads due to the reduced flange height. In Fig. 22(b), the impact of the compressed joints’ shorter flange height is depicted.

As a lower force of 60 kN was applied to compress the 3-branch joints compared to the 100 kN for the No-branch joints, the flange height is higher in the 3-branch post-compression configuration. This difference justifies why compression had a lesser impact on the force-displacement curves for these joints compared to the branch-less joints. Additionally, the flange length (F) for 3-branch joints was already higher due to process design limitations. Consequently, both pre- and post-compression joints of this configuration exhibit better mechanical performance than the branch-less configuration joints.

Joint failure occurs due to different mechanisms depending on the joint configuration. For 3-branch joints, failure happens due to crack propagation around the branch edges, caused by very high stress concentrations. On the other hand, for branch-less joints, failure occurs when the outer sheet flange no longer impedes the movement of the

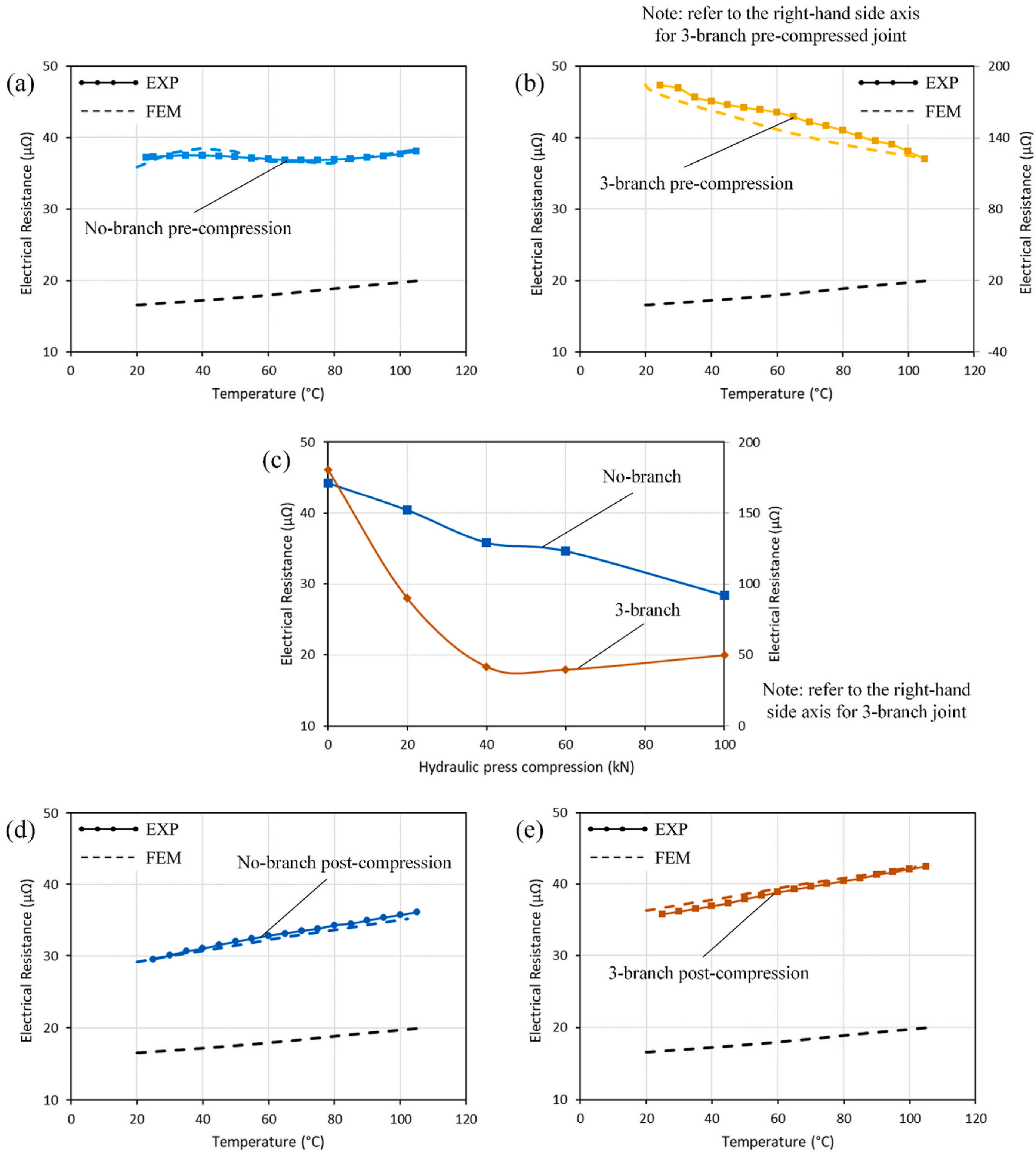

Fig. 20. (a) Experimental and numerically predicted influence of temperature in joints electrical resistance for No-branch pre-compression joints and for (b) 3-branch pre-compression joints, (c) pressure's influence on joints electrical resistance at ambient temperature ($T = 20^{\circ}C$), (d) experimental and numerically predicted influence of temperature in joints electrical resistance for No-branch post-compression joints and for (e) 3-branch post-compression joints.

inner sheet around the bearing area, leading to sheet dismount. This failure mechanism is known as hole bearing.

In Fig. 22(c) and (d), the maximum initial and end load averaged values obtained for pre- and post-compression joints are presented, respectively. The error bars indicate the standard deviation obtained across several joint tests. Pre-compression, 3-branch joints reached a maximum shear load of 4.53 kN and 13.84 mm displacement, while branch-less joints achieved 3.56 kN and 9.30 mm, respectively. After compression, 3-branch joints showed a maximum shear load and displacement of 3.79 kN and 6.39 mm, respectively. In contrast, branch-less joints after compression sustained lower loads and displacements, with the best joint reaching 3.05 kN of maximum shear load and 6.12

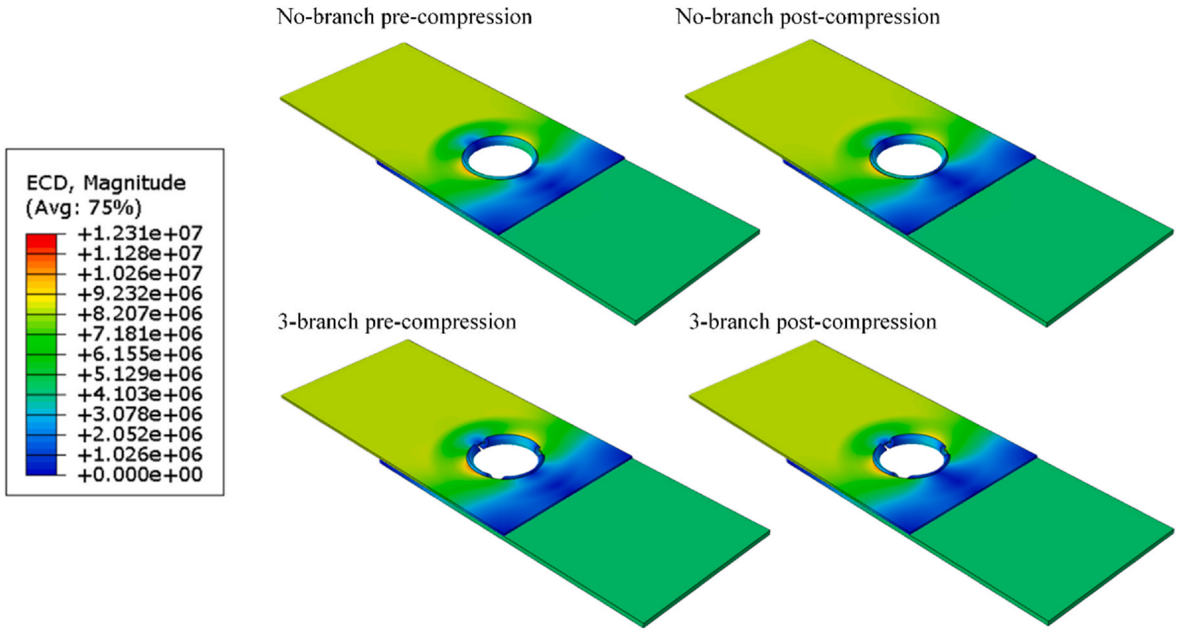

Fig. 21. Electric current density [A/mˆ2] for pre- and post-compression joints with and without branches at a current spike stage at a temperature of around 85 °C.

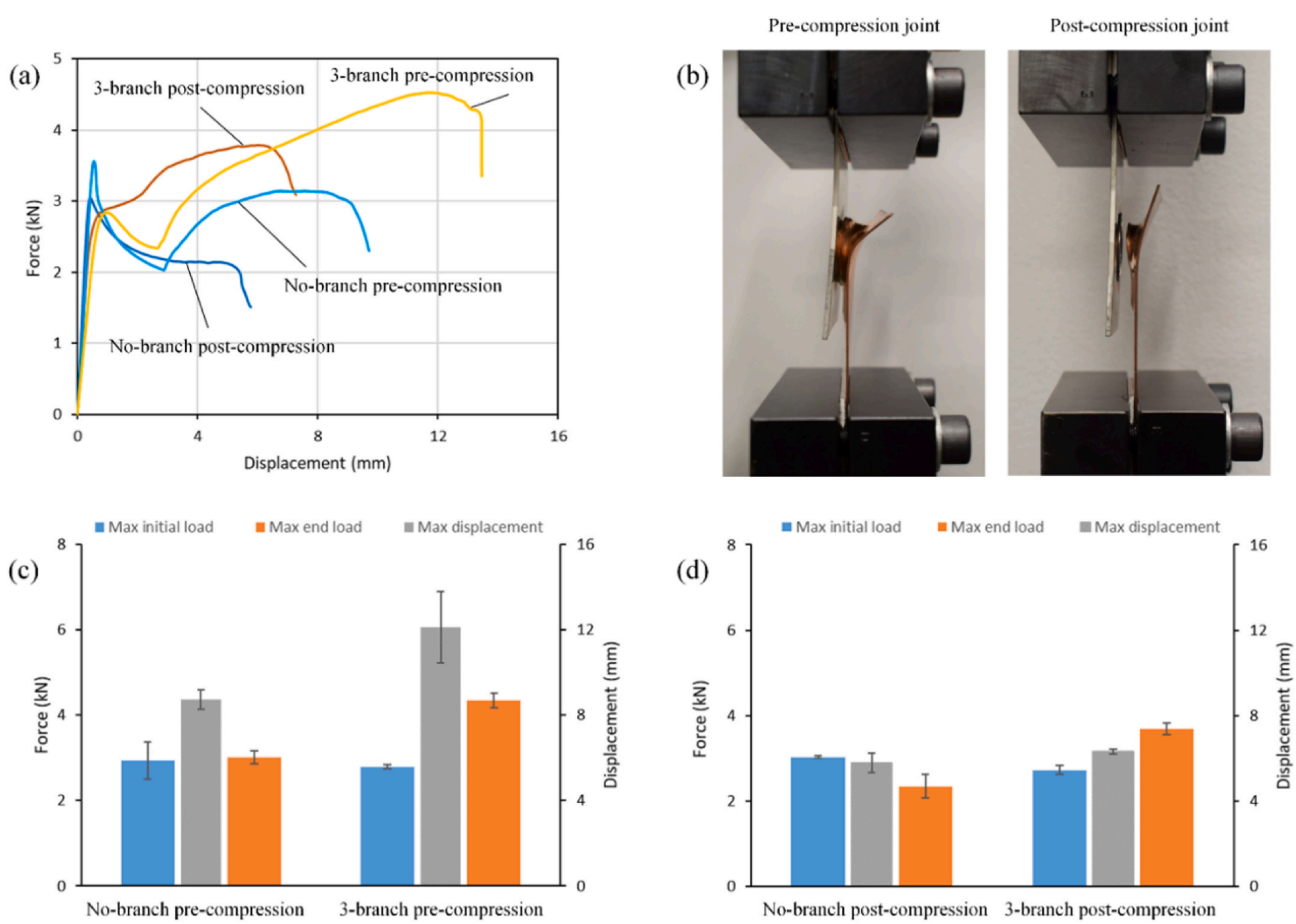

Fig. 22. (a) Shear force - displacement test curves for the four joint types: pre- and post- No- and 3-branch joints, (b) pre- and post-compression joints at the end stage of the shear test, (c) maximum initial shear load, end shear load and displacement for pre-compression joints, (d) maximum initial shear load, end shear load and displacement for post-compression joints.

mm maximum displacement.

6. Conclusions

This paper presents novel joints produced by an innovative joining technique called hole hemming, aimed at joining two dissimilar aluminium and copper strips for potential hybrid busbar manufacturing. The study demonstrated that an increase in thickness ratio resulted in higher electrical resistance with increasing temperature. Similarly, the inclusion of holes in the joint configuration also increased electrical resistance across all temperatures. Two models were simulated to approximate finite element analysis to experimental joint testing, before and after the compression manufacturing step. The numerical models were validated through direct comparison with experimental tests of the electrical resistance-temperature behaviour. An increase in electrical resistance compared to ideal joints was expected and observed.

A study on the influence of pressure was conducted due to the known impact of pressure on electric current flow behaviour in a joint. At ambient temperature, it was found that a 60 kN hydraulic press compression improved the current flow in 3-branch joints by decreasing electrical resistance by 78.1 %. In the case of No-branch joints, a decrease of 35.9 % was observed. The same joints were subjected to a destructive shear test. Results showed that pre-compression joints sustained higher loads and displacements, with values around 4.53 kN of maximum shear load and 13.84 mm maximum displacement for 3-branch joints, and 3.56 kN and 9.30 mm, respectively, for maximum shear load and displacement in the case of branchless joints. Although lower values were obtained for joints after hydraulic press compression, the significantly improved current flow behaviour compensated for the slightly reduced mechanical performance. Post-compression branchless joints exhibited electrical resistance intervals of 29.51–36.07 μΩ and 35.80–42.13 μΩ over a temperature range of 25–105 °C, with a linear increase in electrical resistance. Despite the inherent decrease in resistance due to the reduced material in the joint characteristic of HH joints, the results are promising. This joining technique requires no additional elements, materials, or welding techniques, thereby avoiding additional weight, cost, and any adverse effects on the thermal and electrical properties of the materials. In conclusion, this technique shows great potential for integration into hybrid busbar manufacturing operations tailored for electric vehicle battery applications. However, the investigation primarily focuses on static conditions, without considering the effects of mechanical loads, vibrations, or long-term degradation on the thermal-electrical performance of the joints. Additionally, the joints have not yet been tested within a battery pack for interconnecting battery modules. Future work will address these aspects to provide further insights into the capabilities of the proposed interconnections for hybrid busbars.

CRediT authorship contribution statement

D.P.M. da Costa: Writing – original draft, Visualization, Validation, Software, Methodology, Investigation, Formal analysis, Data curation. **M.M. Kasaei:** Writing – review & editing, Visualization, Validation, Supervision, Software, Project administration, Methodology, Investigation, Formal analysis, Conceptualization. **R.J.C. Carbas:** Writing – review & editing, Validation, Supervision, Resources, Methodology, Investigation. **E.A.S. Marques:** Writing – review & editing, Resources, Investigation. **R.F.V. Sampaio:** Writing – review & editing, Validation, Resources, Methodology, Investigation. **I.M.F. Bragança:** Writing – review & editing, Validation, Resources, Methodology, Investigation. **L.F. M. da Silva:** Writing – review & editing, Supervision, Project administration, Funding acquisition.

Declaration of competing interest

The authors declare that they have no known competing financial interests or personal relationships that could have appeared to influence the work reported in this paper.

Acknowledgements

DPM da Costa, MM Kasaei, RJC Carbas, EAS Marques and LFM da Silva gratefully acknowledge the funding provided by Fundação para a Ciência e a Tecnologia (FCT), Portugal, for the project PTDC/EME-EME/6442/2020 and for the scientific employment grant CEECIND/03276/2018. IMF Bragança and RFV Sampaio would like to acknowledge the support provided by Fundação para a Ciência e a Tecnologia of Portugal (FCT) and IDMEC through financial support from the project LAETA Base Funding (DOI: 10.54499/UIDB/50022/2020) and PTDC/EMEEME/0949/2020. RFV Sampaio would also like to acknowledge the support under the PhD Studentship 2022.12351.BD.

Data availability

Data will be made available on request.

References

[1] El-Iali AE, Doumiati M, Machmoum M. Optimal sizing of the energy storage system for plug-in fuel cell electric vehicles, balancing costs, emissions and aging. J Energy Storage 2024;92:112095. 2024/07/01.
[2] Arnold F, Lilienkamp A, Namockel N. Diffusion of electric vehicles and their flexibility potential for smoothing residual demand — a spatio-temporal analysis for Germany. Energy (Calg) 2024;308:132619. 2024/11/01.
[3] El Bakkari F, Mounir H. Compatible alternative energy storage systems for electric vehicles: review of relevant technology derived from conventional systems. Energy (Calg) 2024;288:129775. 2024/02/01.
[4] Shirkhani M, et al. A review on microgrid decentralized energy/voltage control structures and methods. Energy Rep 2023/11/01/2023;10:368–80.
[5] Capasso C, Iannucci L, Patalano S, Veneri O, Vitolo F. Design approach for electric vehicle battery packs based on experimentally tested multi-domain models. J Energy Storage 2024;77:109971. 2024/01/30.
[6] Zuo W, Li D, Li Q, Cheng Q, Zhou K, E J. Multi-objective optimization of multi-channel cold plate under intermittent pulsating flow by RSM and NSGA-II for thermal management of electric vehicle lithium-ion battery pack. Energy (Calg) 2023;283:129085. 2023/11/15.
[7] Wang C, Chen Y. Unsupervised dynamic prognostics for abnormal degradation of lithium-ion battery. Appl Energy 2024;365:123280. 2024/07/01.
[8] Talluri T, Angani A, Shin k, Hwang M-H, Cha H-R. A novel design of lithium-polymer pouch battery pack with passive thermal management for electric vehicles. Energy (Calg) 2024;304:132205. 2024/09/30.
[9] Sampaio RFV, Pragana JPM, Bragança IMF, Silva CMA, Martins PAF. Thermo-electrical performance of hybrid busbars: an experimental and numerical investigation. Proc Inst Mech Eng Part L 2022;237(1):70–80. 2023/01/01.
[10] Kalkan O. Thermal performance improvement of an air-cooled 18650 NMC battery module: a novel busbar design that acts as a turbulator. J Energy Storage 2024;88:111613. 2024/05/30.
[11] Sampaio RFV, et al. Busbars for e-mobility: state-of-the-Art review and a new joining by forming technology. In: *Mechanical and industrial Engineering*(Materials forming, machining and tribology; 2022. p. 111–41.
[12] Pragana JPM, Baptista RJS, Bragança IMF, Silva CMA, Alves LM, Martins PAF. Manufacturing hybrid busbars through joining by forming. J Mater Process Technol 2020;279.
[13] Rücker F, Figgener J, Schoeneberger I, Sauer DU. Battery electric vehicles in commercial fleets: use profiles, battery aging, and open-access data. J Energy Storage 2024;86.
[14] Yetik O, Karakoc TH. Estimation of thermal effect of different busbars materials on prismatic Li-ion batteries based on artificial neural networks. J Energy Storage 2021;38.
[15] Huang Z, et al. An online evaluation model for mechanical/thermal states in prismatic lithium-ion batteries under fast charging/discharging. Energy (Calg) 2024;302(2024/09/01):131877.
[16] Zhou L, et al. Optimization of thermal non-uniformity challenges in liquid-cooled lithium-ion battery packs using NSGA-II. Journal of Electrochemical Energy Conversion and Storage 2024;22(4).
[17] Wang H, et al. A thermal network model for multichip power modules enabling to characterize the thermal coupling effects. IEEE Trans Power Electron 2024;39(5):6225–45.
[18] Wong SK, Li K, Rui X, Fan L, Ouyang M, Feng X. Mitigating thermal runaway propagation in high specific energy lithium-ion battery modules through nanofiber aerogel composite material. Energy (Calg) 2024;307:132353. 2024/10/30.
[19] Zhao H, Zhao G, Liu F, Xiang T, Zhou J, Li L. Realizing dendrite-free lithium deposition with three-dimensional soft-rigid nanofiber interlayers. J Colloid Interface Sci 2024;666:131–40. 2024/07/15.

[20] Kim M-J, Bak S-H, Jung W-C, Hur D-J, Ko D-S, Kong M-S. Improvement of heat dissipation characteristics of Cu bus-bar in the switchboards through shape modification and surface treatment. Energies 2019;12(1).
[21] Das A, Li D, Williams D, Greenwood D. Joining technologies for automotive battery systems manufacturing. World Electric Vehicle Journal 2018;9(2).
[22] Das A, Ashwin TR, Barai A. Modelling and characterisation of ultrasonic joints for Li-ion batteries to evaluate the impact on electrical resistance and temperature raise. J Energy Storage 2019/04/01/2019;22:239–48.
[23] Zhang C, Li L. A coupled thermal-mechanical analysis of ultrasonic bonding mechanism. Metall Mater Trans B 2009;40(2):196–207.
[24] Brand MJ, Schmidt PA, Zaeh MF, Jossen A. Welding techniques for battery cells and resulting electrical contact resistances. J Energy Storage 2015;1:7–14.
[25] Sadeghian A, Iqbal N. A review on dissimilar laser welding of steel-copper, steel-aluminum, aluminum-copper, and steel-nickel for electric vehicle battery manufacturing. Opt Laser Technol 2022;146:107595. 2022/02/01.
[26] Kasaei MM, Beygi R, Carbas RJC, Marques EAS, da Silva LFM. A review on mechanical and metallurgical joining by plastic deformation. Discover Mechanical Engineering 2023;2(1):5. 2023/04/27.
[27] Meschut G, et al. Review on mechanical joining by plastic deformation. Journal of Advanced Joining Processes 2022;5:100113. 2022/06/01.
[28] Afonso RM, Alves LM. Double-sided self-pierce riveting: electro-mechanical analysis of dissimilar Al-Cu half-lap butt joints. Metals 2023;13(8):1472.
[29] Pragana JPM, Sampaio RFV, Bragança IMF, Silva CMA, Martins PAF. Injection lap riveting of aluminum busbars—A thermo-electro-mechanical investigation. Journal of Manufacturing and Materials Processing 2022;6(4):74.
[30] J. P. Pragana, R. F. Sampaio, R. G. Clara, I. M. Bragança, C. M. Silva, and P. A. Martins, "A new deformable self-clinching fastener," Proc Inst Mech Eng Part L, vol. 0, no. 0, p. 14644207241236463.
[31] Kasaei MM, da Silva LFM. Joining sheets made from dissimilar materials by hole hemming. Proc Inst Mech Eng Part L 2022;236(6):1321–32.
[32] Pereira JAC, Kasaei MM, Carbas RJC, Marques EAS, Lim H, da Silva LFM. Joining magnesium and aluminum alloy sheets by a novel hole hemming process. Thin-Walled Struct 2023;187.
[33] Kasaei MM, Pereira JAC, Carbas RJC, Marques EAS, da Silva LFM. Ductile fracture prediction in hole hemming of aluminum and magnesium sheets. Metals 2023;13 (9):1559.
[34] Kasaei MM, Carbas RJC, Marques EAS, da Silva LFM. A novel joining technology for metal and polymer sheets. Journal of Advanced Joining Processes 2024;9.
[35] Haran-Nogueira A, et al. Development of hybrid bonded-hole hemmed joints: process design and joint characterization. J Manuf Process 2023;95:479–91.
[36] Haran-Nogueira A, Kasaei MM, Akhavan-Safar A, Carbas RJC, Marques EAS, da Silva LFM. Failure analysis of hybrid bonded-hole hemmed joints for dissimilar materials. Thin-Walled Struct 2023;189:110907. 2023/08/01.
[37] da Silva BFA, Kasaei MM, Akhavan-Safar A, Carbas RJC, Marques EAS, da Silva LFM. Failure analysis of novel hybrid busbars made by hole hemming for electric vehicle applications. Arch Civ Mech Eng 2025;25(2):107. 2025/03/05.
[38] da Silva BFA, Kasaei MM, Akhavan-Safar A, Carbas RJC, Marques EAS, da Silva LFM. Failure behavior of hole hemmed joints with a novel configuration for hybrid busbars in electric vehicle batteries. Eng Fail Anal 2025;167:109019. 2025/01/01.
[39] da Silva BFA, Kasaei MM, Akhavan-Safar A, Carbas RJC, Marques EAS, da Silva LFM. Fatigue analysis of novel hole hemmed joints for hybrid busbars in electric vehicle batteries. Eng Fract Mech 2024;311:110590. 2024/11/25.
[40] Millan P, et al. On the influence of joining processes on the vibration of structures. Journal of Advanced Joining Processes 2023;8:100170. 2023/11/01.
[41] IEEE standard for metal-clad switchgear. 2015.
[42] Costa DP Md. Development of the novel hole hemming process for manufacturing hybrid busbars in electric vehicle batteries. Master, mechanical engineering department. University of Porto; 2024.
[43] da Costa DPM, Kasaei MM, Carbas RJC, Marques EAS, da Silva LFM. A novel joining technology for hybrid busbars in electric vehicle batteries. Thin-Walled Struct 2024;205:112590. 2024/12/01.
[44] Conceição AGC, Kasaei MM, Carbas RJC, Marques EAS, da Silva LFM. A flexible tool for joining dissimilar materials by the novel hole hemming process. Mech Base Des Struct Mach 2023:1–29.
[45] Kumar N, Masters I, Das A. In-depth evaluation of laser-welded similar and dissimilar material tab-to-busbar electrical interconnects for electric vehicle battery pack. J Manuf Process 2021;70:78–96. 2021/10/01.
[46] User's Manual.6.7.3 ABAQUS. Coupled thermal-electrical analysis. VOLUME II. ANALYSIS 2014:1–6.
[47] Das A, Masters I, Haney P. Modelling the impact of laser micro-joint shape and size on resistance and temperature for electric vehicle battery joining application. J Energy Storage 2022;52.
[48] Poplavko YM. Metals. Electronic Materials 2019:165–220.